Petrological Evolution and Mass Redistribution in Basaltic Fault Zones: An Example from the Faroe Islands, North Atlantic Igneous Province

Bob Bamberg[1], Marc K. Reichow[1], Richard J. Walker[2], Audrey Ougier-Simonin[3]

[1]School of Geography, Geology and the Environment, University of Leicester, University Road, Leicester LE1 7RH, UK

[2]Department of Earth and Planetary Sciences, University of California, Davis, 1 Shields Avenue, Davis, California 95616, USA

[3]Rock Mechanics and Physics Laboratory, British Geological Survey, Nicker Hill, Keyworth, Nottingham NG21 5GG, UK

B Bamberg: bobbamberg@gmail.com (corresponding author)
MK Reichow: mkr6@le.ac.uk
RJ Walker: rjwalker@ucdavis.edu
A Ougier-Simonin: audreyo@bgs.ac.uk

Key Points

- Basaltic fault zones record isochemical alteration in the damage zone and mechanical mixing in the fault core.
- Only Ca, Si, Al, and CO_2 are mobilized. They are dissolved in the damage zone and precipitated as zeolites and calcite in the fault core.
- Fault cores appear to evolve as chemically and hydraulically closed systems, and only CO_2 is added during damage zone alteration.

This manuscript is a preprint submitted to **Geochemistry, Geophysics, Geosystems** and has not yet undergone peer-review. If accepted, the published version may include slight changes to the text and figures, and can be accessed via a link on the article webpage.

Abstract

Fault rock petrology exerts an important control on the permeability structure and mechanical properties of fault zones. Slip-related deformation on upper crustal faults in basaltic rocks is closely associated with fluid-rock interaction, altering the distribution of physical properties within the fault. Here we present the first quantitative description of the geochemical and petrological evolution of basalt-derived fault rocks, from three passively exhumed fault zones in the Faroe Islands, on the European Atlantic Margin. Fault-rock petrology is determined by optical petrography and automated phase identification based on micrometer-scale chemical maps from scanning electron microscope X-ray spectroscopy. Geochemical evolution is assessed from major and trace element composition measured by X-ray fluorescence. The fault rocks show intense isochemical alteration from a tholeiitic basalt protolith in the damage zones, and mechanical mixing in the fault cores. Pervasive alteration occurs early during fault zone evolution, with incipient fault damage increasing permeability, and allowing along-fault percolation of carbonated meteoric water, increasing fluid-rock ratios. Our results suggest the only mobile species within the fault zones are Ca, Si, Al, which are leached during hydrolysis of volcanic glass and plagioclase, and CO_2, which is added by percolating waters. These species are transported from the damage zones into the fault cores, where they precipitate as zeolite and calcite cements in veins and hydrothermal breccias. We find no evidence of gross chemical gain or loss apart from CO_2, hence propose that solutes are replenished by cement dissolution through pressure-solution during cataclastic creep, during repeated cycles of hydrofracture and cementation.

1 Introduction

Basalt is the most common volcanic rock type on Earth (Winter, 2001), and holds great potential to reduce CO_2 concentration in our atmosphere. Basalts can act as a major carbon sink through metal carbonation (Matter et al., 2016; Snæbjörnsdóttir et al., 2020; Lewis et al., 2021) or through intercrystalline adsorption (Stillings et al., 2023). Additionally, the commonly elevated geothermal gradients in basalt formations can be tapped to provide sustainable geothermal energy (Marieni et al., 2018). Faults constitute an important heterogeneity in basaltic sequences, and their stability and permeability is strongly controlled by fault-internal petrological evolution (Walker et al., 2013b; Frolova et al., 2014). Basalt alteration through reaction with residual fluids is thought to start immediately after emplacement during the cooling process (e.g. Mattioli et al., 2016). Alteration commonly takes the form of partial plagioclase replacement (Schenato et al., 2003), and dissolution of volcanic glass and primary minerals, especially olivine, and precipitation of various clay and zeolite minerals, and sometimes calcite, in vesicles (Kristmannsdóttir, 1979; Triana et al., 2012; Mattioli et al., 2016). Early alteration with residual fluids immediately after emplacement is followed by alteration with hydrothermal fluids, and/or meteoric or sea water (Alt and Honnorez, 1984; Schenato et al., 2003; Frolova et al., 2014; Mattioli et al., 2016). Petrological characterizations of fault zones within basalt are scarce but indicate much more extensive alteration than in the surrounding host basalt (Walker et al., 2012; 2013a; 2013b). Such pervasive alteration can have profound implications for fault zone permeability and stability, where interconnected and permeable zeolite veins, and impermeable clay networks may result in a mixed barrier-conduit permeability structure (Walker et al., 2013a; Walker et al., 2013b). In addition, the pervasive replacement of frictionally strong feldspar-dominated assemblages by weaker zeolites

(Yukselen-Aksoy, 2010; Frolova et al., 2014) or clay minerals (Shimamoto and Logan, 1981; Haines et al., 2013; Boulton et al., 2014; Carpenter et al., 2016) can promote mechanical weakening of the fault zone. The structure of the faults analyzed in this study also indicates that fault stability is strongly controlled by fluid pressure evolution and thus permeability structure of the fault (Bamberg et al., 2022).

In this study, we seek to characterize the petrological and geochemical evolution within basalt-hosted fault zones, and integrate these into a conceptual physicochemical model for fault evolution in shallow basalts (Bamberg et al., 2022). Chemical mobility and mass balance within the fault are calculated from X-ray fluorescence whole rock geochemistry. The petrological evolution of the fault zone is reconstructed through optical petrography and high-resolution, automated phase mapping based on X-ray spectrometry in a scanning-electron microscope. To the best of our knowledge, this represents the first systematic petrological and geochemical characterization of basalt-derived fault rocks. We sampled three exceptionally well-exposed fault zones in the Faroe Islands Figure 1, that span a displacement range from 30 m to, potentially, kilometer-scale (Bamberg et al., 2022), and cover a full transect of fault rocks, including undeformed protolith, damage zone, fault core, and principal slip zone. Our results indicate that the studied faults evolved as a hydrochemically closed system, trapping carbonated meteoric fluids. Initial pervasive alteration in the damage zone combined with comminution during strain accumulation appear to promote compartmentalization of the fault core, limiting petrological evolution to zeolite and calcite precipitation and dissolution without communication to external fluid sources.

2 Geology of the Faroe Islands

The Faroe Islands (Figure 1A) are an archipelago located on the European continental shelf of the NE-Atlantic Ocean, between the Shetland Islands and Iceland. They were emplaced in the Paleogene, during the initial outburst of the Icelandic Plume before the onset of Atlantic rifting, and are part of the North Atlantic Large Igneous Province (Ritchie and Hitchen, 1996). The Faroes stratigraphy is dominated by the tholeiitic basalts of the Faroe Islands Basalt Group, which are subdivided into seven formations (Passey and Bell, 2007; Passey and Jolley, 2008), with a maximum total stratigraphic thickness of ca. 6.6 km (Figure 1B) (Waagstein et al., 1984; Chalmers and Waagstein, 2006; Passey and Bell, 2007). $^{40}Ar/^{39}Ar$ (Hansen et al., 2002; Storey et al., 2007) and K/Ar & $^{40}Ar/^{39}Ar$ (Waagstein et al., 2002) indicate emplacement between 60 Ma and 55 Ma. The Faroes stratigraphy is summarized in Figure 1B and described in detail by Rasmussen and Noe-Nygaard (1970), Waagstein et al. (1984), and Passey and Jolley (2008). The faults described in this study are hosted in the extensive sheet lobes of the Beinisvørð Formation (Í Botni fault zone: Figure 1B & D), the compound lavas of the Malinstindur Formation (Gøtugjógv fault zone: Figure 1B & C), and the simple lavas of the Enni Formation (Selatrað fault zone: Figure 1B & C).

The younger basalts of the Malinstindur and Enni Formations (Figure 1B) have been subdivided geochemically into two main groups: low-Ti lavas (TiO_2 < 1.95 wt.%) depleted of incompatible elements, and high-Ti lavas (TiO_2 > 1.95 wt.%) with enriched incompatible element abundances (Gariépy et al., 1983; Hald and Waagstein, 1991; Holm et al., 2001; Søager and Holm, 2009). Both types are dominated by plagioclase-phyric basalts, but about 15 % of low-Ti lavas are olivine-phyric basalts or picrites (Hald and Waagstein, 1991; Holm et al., 2001). A few less-common basalts have also been described,

with either intermediate Ti concentrations, high Ti and high Mg (>10 %), or contaminated with lower crustal material (Holm et al., 2001). The Malinstindur formation is dominantly composed of plagioclase-phyric high-Ti basalts (Holm et al., 2001; Søager and Holm, 2009). The lower parts of the Enni formation are dominated by phyric and aphyric low-Ti basalts in the north of the archipelago, and by phyric high-Ti basalts in the south. The upper part of the stratigraphically youngest Enni formation is composed of both aphyric high-Ti and low-Ti basalts. The high-Ti lavas have been further subdivided into three stratigraphically distinct units, based on their Nb, Zr, and Y concentrations, and can be correlated to lavas in East Greenland (Søager and Holm, 2009). This shows that volcanic activity continued on both sides of the Atlantic Rift, even after the magmatic center moved away from the Faroe Islands (Søager and Holm, 2009).

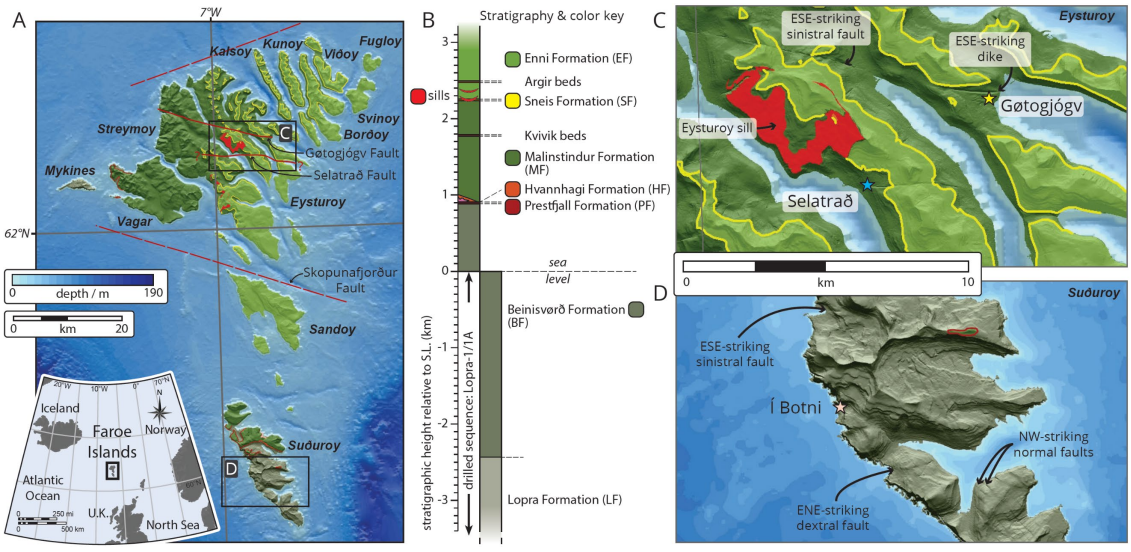

Figure 1. (A) Geological map of the Faroe Islands. Red, dashed lines indicate the proposed locations of large displacement ENE-WSW (unnamed north coast fault; Walker et al., 2011), and ESE-WNW (Skopunafjordur fault; Passey, 2009) faults that bound the Northern Islands. (B) Vertical stratigraphic section through the Faroe Island Basalt Group (from Passey and Bell, 2007). Close-up maps highlight the local topography and geology of the (C) Gotugjogv, Selatrad, and (D) I Botni fault zones. See key in B.

3 Methods

Automated phase identification and microtexture imaging were performed on a ZEISS Sigma 300 Field emission - analytical scanning electron microscope (SEM). Polished and carbon-coated (ca. 30 nm) thin sections were analyzed under high vacuum (ca. 1.0×10^{-5} Pa) using a 15 kV accelerating voltage (suitable for silicate minerals) and a 120 µm beam aperture. Imagery was captured via a high-definition backscattered electron detector (BSE). Chemical composition was determined via energy dispersive X-Ray spectrometry (EDS) utilizing two Bruker XFlash|60 EDS detectors, that are positioned perpendicular to one another to prevent data shadowing effects, with a 1.25 µm beam step and a dwell time of 8 µs. The chemical compositions were calculated using a standardless P/B-ZAF quantification method via Bruker Esprit 2.1. Element concentration data are only semi-quantitative as no reference material was used for calibration. Automated phase identification was performed using ZEISS Mineralogic software. The chemical composition of each analysis (i.e., pixel) is compared to the compositional ranges in a user-defined, hierarchical phase list (recipe; see Table A-1 in Appendix), and assigned the first matching phase. Phase selection and compositional ranges for this recipe are based on literature review and petrographic characterization, and are improved in an iterative process to match the phase compositions in the samples. The process is similar to manual phase identification in SEM-EDS data, but automatically applied to the whole dataset.

Whole rock geochemistry was determined using a PANanalytical Axios Advanced wavelength dispersive X-ray fluorescence spectrometer. Major element and volatile concentration was determined in fusion beads prepared from ignited powders with a sample to flux ratio of 1/5. Loss on ignition (LOI) was determined after ignition at 950 °C in air for 1 h of the pre-dried powders. Trace elements were measured in pressed powder pellets with

7.5 g sample material bound with 15–20 drops polyvinyl alcohol. Detection limits for major elements, as defined from blank analysis, are usually better than 0.1 wt.%. Calibrations were set using a suite of 9 international and internal rock reference materials for major elements and 17 reference materials for trace elements (data provided in data repository Bamberg, 2023). Analytical uncertainties of our data are between 0.3 and 3.2 %, except for MnO (49.4 %) and SO_3 (48.3 %), and 1–8 % for major and trace elements, respectively. Major and trace element analytical results for the Faroe Island samples are provided in Table 1 and Table A-2 and selected reference materials in Appendix Table A-3 to Table A-5.

4 Data Analysis

4.1 Fault Zone Meso- & Microtexture

The three fault zones analyzed in the Faroe Islands have up to decameter-wide damage zones surrounding meter-wide fault cores that contain multiple cataclastic shear bands and low-strain lenses organized around a central slip zone. Damage associated with the low-displacement fault zone in Í Botni (IBO: location in Figure 1D, detail in Figure 2) consists of a range of variably altered cataclastic breccias (Figure 2B) within the fault zone, grading back to undeformed host rock through a zone of chaotic, mosaic, and crackle breccias (Figure 2B,C). In the large-displacement Gøtugjógv (GOT: location in Figure 1C, detail in Figure 3) and Selatrað (SEL: location in Figure 1C, detail in Figure 4) fault zones, distributed fracturing in the damage zone is characterized by high concentrations of meter- to decameter-scale fractures and secondary faults. A structural framework is provided by Bamberg et al. (2022), including fault and fracture distribution, geometry, and deformation mechanisms, hence we summarize those aspects here to focus on petrological changes.

193

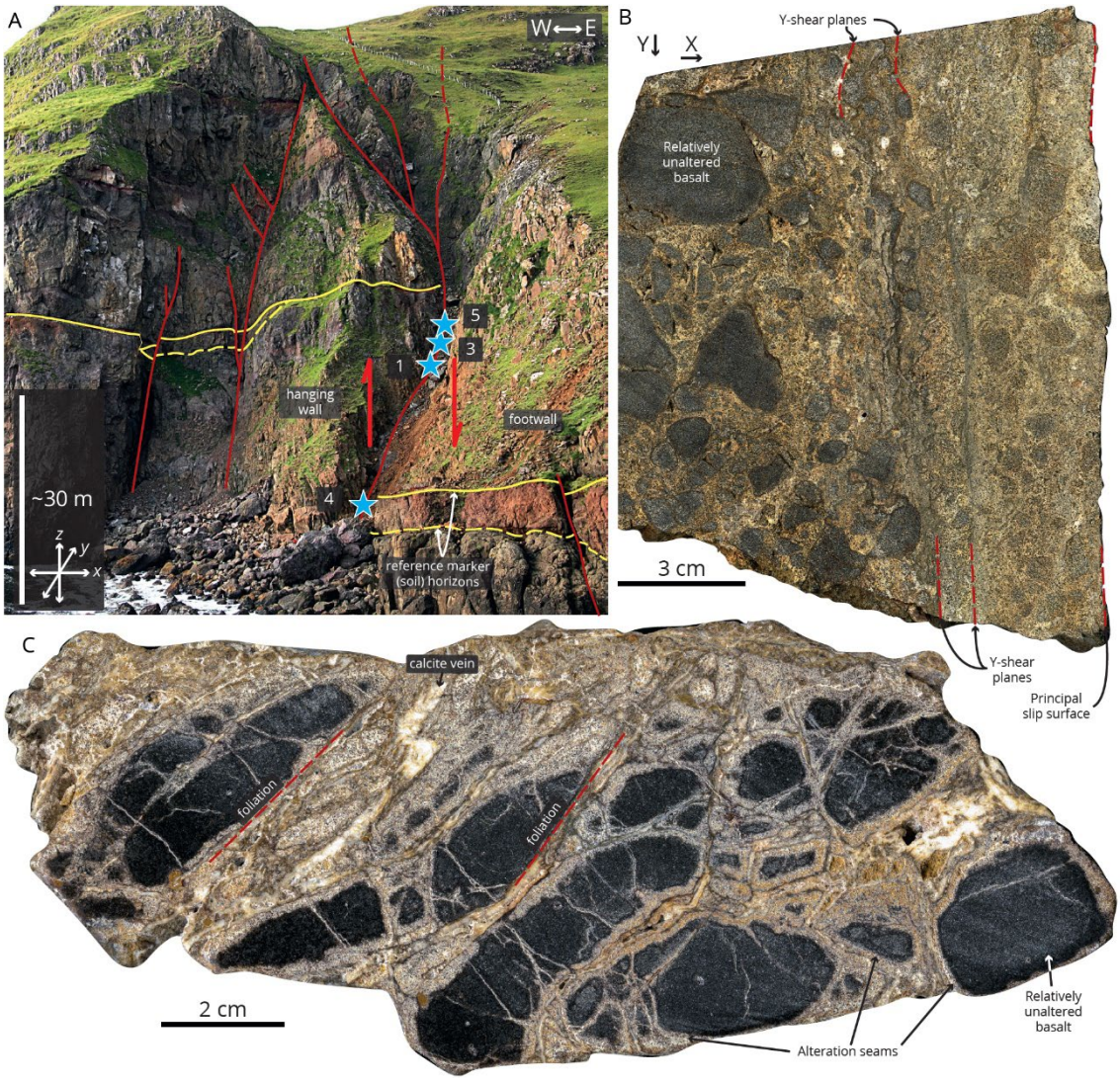

194

195 Figure 2. (A) The I Botni fault zone on Suduroy is a 50 m wide normal fault with 30 m
196 displacement concentrated on the easternmost strand, as indicated by the marker horizon
197 (yellow). Sample locations are indicated by blue stars. (B) The fault core (not shown) is
198 bounded by slip surfaces and cataclastic, chaotic breccias coarsening away from the core.
199 (C) Alteration is limited to the immediate wall rock of fractures and cracks, and rare calcite
200 cements. Localized, black foliation might indicate pressure-solution.
201

202 The unmodified host rock in all localities is a tholeiitic basalt dominated by a plagioclase-

203 pyroxene assemblage including abundant ilmenite and magnetite (Figure 5A & Figure 6A–

204 B). The compound lavas hosting the Gøtugjógv and Selatrað faults can contain <1 cm large

plagioclase phenocrysts, which seem to be absent from the simple lavas in Í Botni. The fine-grained groundmass is composed of opaques (identified as ilmenite and magnetite by SEM-EDS; Figure 6A–B), 50–100 μm large glomerates of anhedral pyroxenes, 100–500 μm long euhedral plagioclase crystals, as well as 50–100 μm large subhedral olivine crystals. The latter have been almost fully replaced by brown, amorphous to fibrous iddingsite ± chlorite (Figure 5A–B). Abundant pockets of brown volcanic glass form an intersertal texture with the plagioclase crystals. The volcanic glass is partially devitrified, often showing radially fibrous rims of a light brown color, enclosing green-brown interior with dark green interference colors (likely representing palagonite), and sometimes a core of zeolite (Figure 5A–C). Vesicles, most common in the porous lava tops, tend to be lined with <50 μm of celadonite ± clay minerals and are filled with coarse zeolite (≤500 μm; Figure 5G & Figure 6C). Optically estimated mineral abundances are: 30 % plagioclase, 35 % pyroxene, 5 % opaques, 10 % olivine and alteration products, and 20 % (devitrified) volcanic glass.

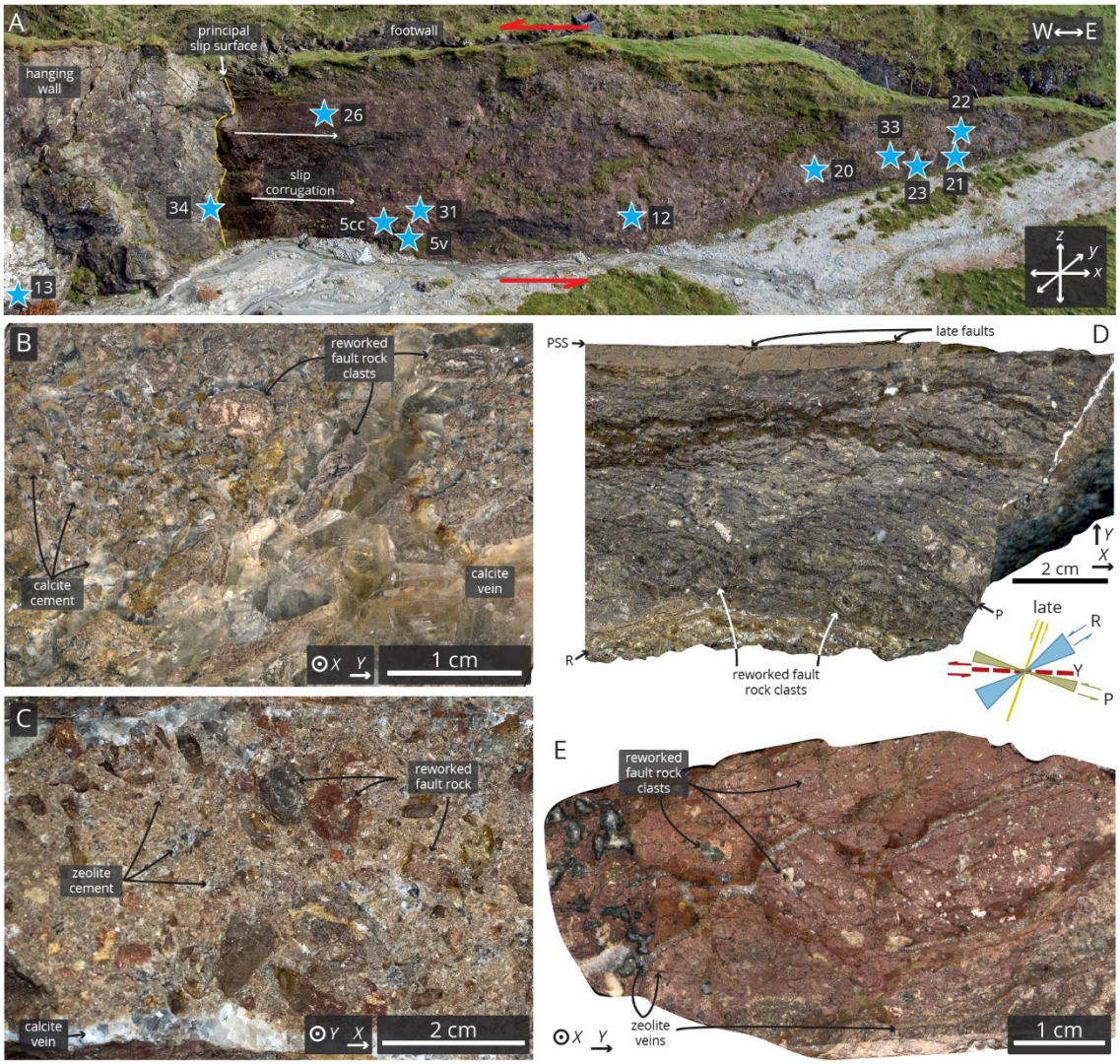

220

221 Figure 3. (A) A 50-m-long and 10-m-high diagonal section through the fault core of a
222 sinistral strike-slip fault zone is exposed near Gotugjogv. The corrugated principal slip
223 surface cuts across a slip zone of lenticular bodies containing fault rock and bounded by
224 cataclasites. Sample locations are indicated by blue stars. The fault core also contains
225 extensive (B) calcite- and (C) zeolite-cemented fault veins that run parallel to the slips
226 surface with angular fault rock fragments. (D) Cataclasites of the slip surface can be
227 strongly foliated, and show late-stage transection of the foliation. (E) Cataclastic bands
228 away from the principal slip surface show signs of reworking such as brecciation by zeolite
229 veins. Clasts of reworked fault rock are common throughout the entire fault core.
230

231 Within the fault damage zones, plagioclase crystals show an increasing concentration of

232 intracrystalline fractures towards the fault core, which are zeolitised as deep as a few

micrometers (Figure 5D). In the vicinity of veins and large-scale fractures, plagioclase breakdown becomes more extensive, and crystal grains are, in some cases, almost entirely replaced (Figure 5F–G). In early stages of faulting, as shown in Í Botni, the damage zone is brecciated approaching the principal slip zone, grading from mosaic to chaotic breccia at the slip zone contact, with centimeter-scale clasts in a comminuted matrix, and in some places, calcite cement (Figure 2B–C). The ≤50 cm wide slip zone itself is bounded by striated and polished slip surfaces. It is dominated by gouge and cataclasite, with weakly altered host rock clasts (Figure 2B–C), commonly up to a 5 mm in diameter, but sometimes as large as 1–2 cm, in a fine-grained matrix (<25 μm). Clast composition and microtexture is similar to the damage zone rocks described above, with preserved basaltic texture, including fractured and partially zeolitised plagioclase. The matrix is composed of altered host rock comminuted to the micrometer scale. Optical discrimination between plagioclase and zeolite in the fine-grained matrix is only possible where plagioclase feldspar displays distinctive polysynthetic twinning, inhibiting an accurate estimation of the degree of zeolitisation. However, albite twins can be observed in some matrix grains, indicating that plagioclase zeolitisation is not complete. Further, a brown microcrystalline-amorphous or fibrous phase is common along fractures, resembling iddingsite replacing olivine. The degree of plagioclase zeolitisation can be quantified using SEM-EDS and is described in the next section.

In larger displacement faults (the Gøtugjógv & Selatrað fault zones), small-scale brecciation, as seen in Í Botni, is rare within the damage zone. Instead, the altered host rock described previously is fractured by meter- to decameter-scale secondary faults and smaller fractures, which are sometimes mineralized with calcite and/or zeolite, closer to the fault

zone. The fault cores are composed of fault rock lenses bounded by cataclastic shear bands, organized around a prominent slip surface (Figure 3A & Figure 4A). These lenses usually contain cataclasites proximal to the slip surface (Figure 3E), and mineralized breccias closer to the damage zone (Figure 3B–C). The shear bands are composed of ultracataclasite (or gouge), as is a <10 cm thick zone around the slip surface (Figure 3D, Figure 4D, Figure 5I–J). Clasts within the breccia tend to preserve primary basaltic textures, with pyroxene glomerates that show little evidence of alteration despite intense fracturing, and glass in the interstitial space is replaced by opaques, zeolites, and diffuse patches of dark red-brown staining over microcrystalline grains and spherulitic–dendritic opaques (identified as ilmenite by SEM-EDS) (similar to proximal damage zone; Figure 5C & H). Some clasts are composed of other fault rocks—breccias or cataclasites—and in some cases contain multiple types of fault rock separated by a sharp contact, such as clast-within-clast textures or fragments of wall rock-vein contacts (Figure 5N–P). These clasts are mostly hosted in well crystallized, millimeter-long bladed zeolite (Figure 5N) and/or <0.5 mm blocky calcite cements (Figure 5O & P). Pore space within zeolite cements is filled with late, coarse (≤1 cm) calcite; typically each pore is filled by a single calcite crystal (Figure 5N). In calcite-cemented breccias, clasts are commonly overgrown with a thin zeolite coating of irregular thickness (<1 mm) (Figure 5O), and the cement also contains pockets of zeolite with the contact either following an idiomorphic calcite grain boundary, or showing calcite growth around the zeolite crystals; sometimes both styles are developed in the same pocket (Figure 5P).

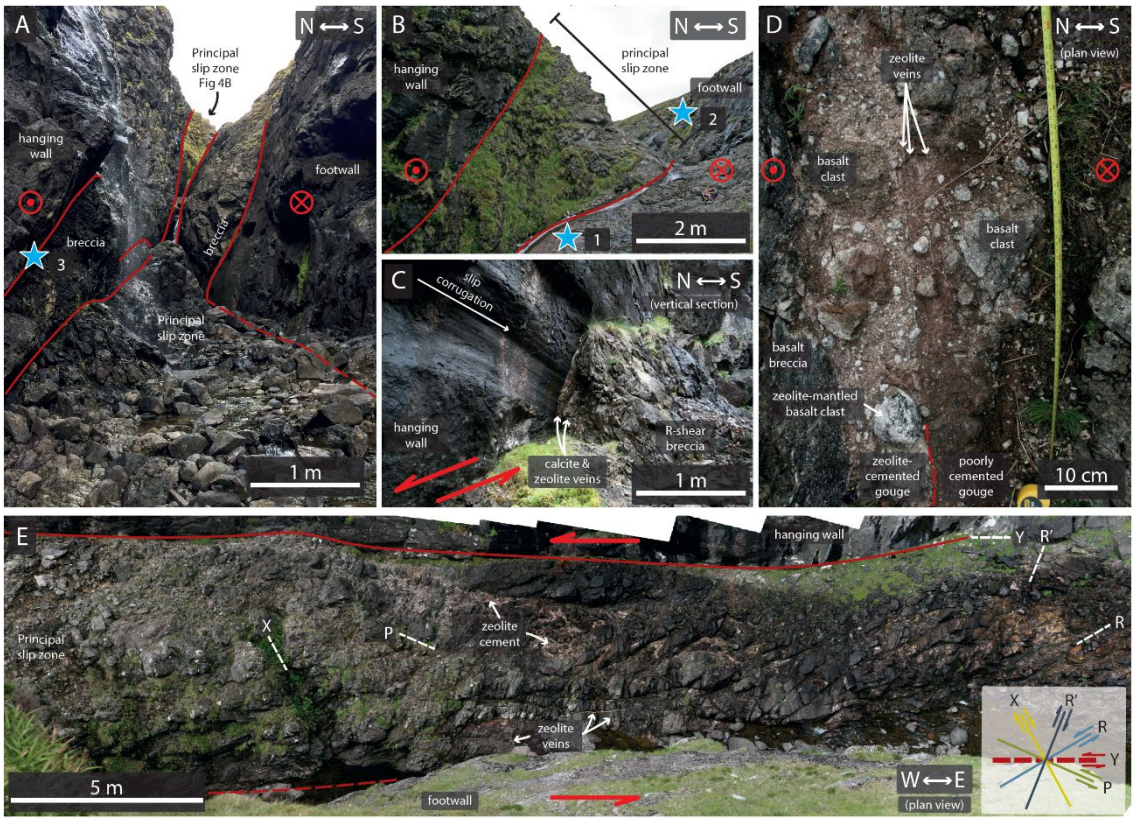

278

279 Figure 4. (A) The sinistral strike-slip fault zone at Selatrad is exposed in a deep and long
280 canyon, where a stream has eroded the fault core. Several (A & B) fault rock lenses and (C)
281 polished and striated slip surfaces can be identified. (D & E) The canyon floor shows the
282 fault core with a decameter-thick principal slip surface composed of partially cemented
283 gouge in the north, next to a (E) highly fractured (following Riedel orientations) meter-
284 thick layer in the south.
285

286 Many cataclasites in Gøtugjógv and Selatrað are foliated on hand-specimen scale, featuring
287 millimeter-wide, dark red-brown bands parallel to Riedel shear orientations (Figure 3D),
288 and manifesting through a diffuse staining of the matrix on the microscale (Figure 5L).
289 Additionally, some cataclasites show microscopical foliation of aligned, light brown-
290 yellow clay bands separating other grains (Figure 5K). Breccias from Í Botni can contain
291 very narrow black foliae between clasts that resemble pressure-solution seams (Figure 2C
292 & Figure 5E). The cataclasite matrix is commonly stained to a dark red-brown color, and
293 dominated by zeolite and clay minerals, mixed with comminuted pyroxene (<25 μm) and

294 opaques (<10 μm) (Figure 5I). High-magnification SEM-BSE micrographs of the
295 cataclasite matrix show a mixture of angular fragments of zeolite and pyroxene, generally
296 1–5 μm in size, and micrometer- to sub-micrometer-scale, very bright fragments of Fe-
297 and/or Ti-oxides, suspended in a matrix with a platy and/or spongy texture and a grain size
298 ≤2 μm, possibly representing clay minerals (Figure 5J). Many clasts are made up of
299 reworked mineral cements from veins and breccias, sometimes including the contact to the
300 wall rock, but also other cataclasites, or even heavily altered host rock remnants and
301 preserved amygdales (Figure 5M–P). Ultracataclasites lining prominent slip surfaces are
302 much more homogeneous and have smaller clasts than all other sampled (ultra-)
303 cataclasites (Figure 5I–J). Some cataclasites further away from this slip surface are
304 extensively fractured and brecciated by a network of non-tabular, well mineralized zeolite
305 ± calcite veins (Figure 5M).
306

307

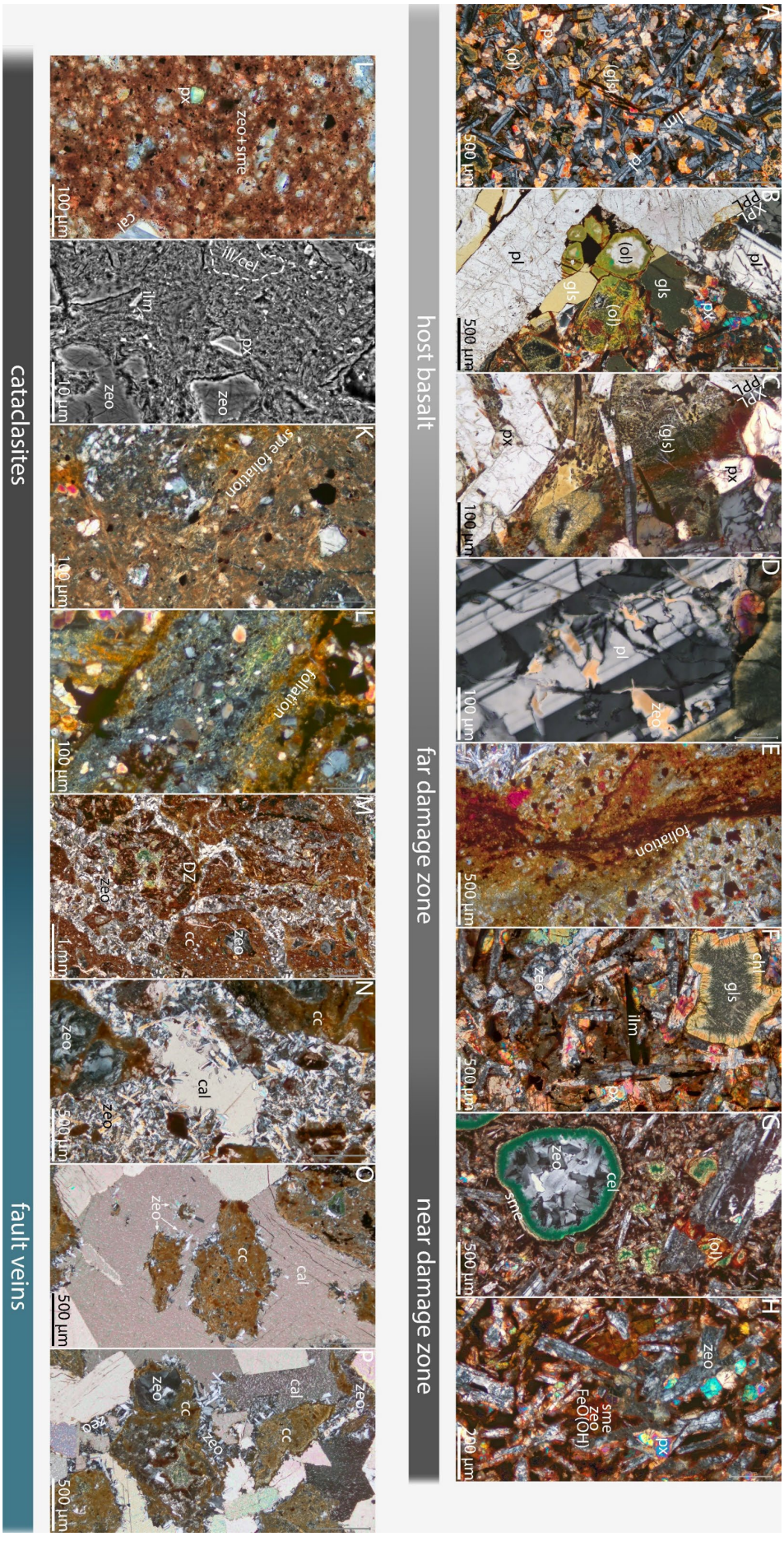
host basalt
far damage zone
near damage zone
cataclasites
fault veins
A
B
C
D
E
F
G
H
I
J
K
L
M
N
O
P
500 µm
100 µm
200 µm
1 mm
(ol)
pl
gls
px
ilm
zeo
cel
sme
cal
cc
chl
FeO(OH)
foliation
ill/cel
zeo+sme
DZ

Figure 5. Petrography of basalt-derived fault rocks. (A) Tholeiitic host basalt; (B) close-up of plagioclase phenocryst with altered volcanic glass and pyroxene in interstitial space (XPL top, PPL bottom); (C) secondary minerals derived from volcanic glass breakdown (XPL top, PPL bottom); (D) zeolitisation (brown) along intracrystalline cracks in plagioclase; (E) localized dark foliation in Í Botni damage zone breccia; (F) altered basalt in damage zone with prominent, devitrified glass (top right corner); (G) celadonite- and heulandite-filled vesicles as well as altered olivine in plagioclase phenocryst; (H) close-up of altered basalt with prominent zeolitised plagioclase laths and red stained interstitial space; (I) highly comminuted and stained ultracataclastic matrix in slip zone, (J) SEM-BSE micrograph of cataclastic matrix; (K) pervasive, clayey foliation in cataclasite; (L) some cataclasites show additional, wide foliation defined by diffuse Fe-staining; (M) brecciated cataclasite with zeolite cement; (N) calcite filling pore in zeolite-cemented fault vein; (O) zeolite overgrowth around clast preceding coarse calcite cementation; (P) complex intergrowth of zeolite and calcite cements in fault vein. Cal – calcite, cc – cataclasite, cel – celadonite, chl – chlorite, DZ – damage zone, gls – volcanic glass [(gls): altered], ilm – ilmenite, ol – olivine [(ol): altered], pl– plagioclase, px – pyroxene, sme – smectite, zeo – zeolite.

4.2 SEM-EDS based Mineralogy

Mineral maps generated from automated phase identification, which were based on element concentrations mapped using EDS, reveal a strong spatial association between plagioclase and zeolite in host and damage zone rocks (Figure 6). Plagioclase grains appear variegated with a network of zeolites and an unclassified mineral phase (Figure 6B–C). Identified zeolites include analcime, most commonly in Gøtugjógv host rock and damage zone, heulandite (more common in the fault core, but also in the Selatrað damage zone sample), or an unspecified zeolite phase which occurs in all samples. Most of this unspecified zeolite phase matches the heulandite classification but with slightly elevated Na and/or reduced Si concentrations. Patches of unclassified material contain individual pixels identified as zeolite, which could indicate that these patches are a zeolitic phase that does not fit into the chemical bounds defined in our recipe (Table A-1 in Appendix). In Í Botni, plagioclase is preserved even in very mature cataclasite next to the slip surface. However, both in Gøtugjógv and Selatrað plagioclase is virtually absent from the fault core (≤ 4 %),

while zeolite concentration is markedly increased compared to the damage zone (Figure 6A).

Pyroxene concentration remains largely consistent after decreasing by about 10–20 % from host rock to damage zone (Figure 6A). This becomes particularly evident when corrections for varying abundances of vein and amygdale cements are taken into account (i.e., normalized to the area excluding heulandite, zeolite, and calcite, but including analcime from plagioclase replacement). A notable outlier is the cataclasite sample from Selatrað, which has a large area of zeolite-cemented plagioclase fragments and reduced pyroxene concentration. Pyroxenes are disseminated throughout the fault rocks, and decrease in size in more mature rock, while maintaining a high angularity (Figure 5 & Figure 6).

SEM-EDS identified most clay minerals in the samples as smectites (i.e., saponite, montmorillonite, or unspecified), illite/celadonite, chlorite, and rare kaolinite (Figure 6). Due to their identical chemical composition, SEM-EDS is unable to distinguish between celadonite and illite, which commonly incorporates Fe and Mg (Deer et al., 2013; Zviagina et al., 2020), hence they are grouped together here. Illite/celadonite is mostly found in the rims of zeolite-filled amygdales in the host rock and damage zone, but also disseminated through fault rocks, though at a very low abundances (Figure 6C–D). The bright green color visible in these zones under an optical microscope indicates that the identified mineral is celadonite rather than illite (Figure 5G). Chlorite concentration is more stable throughout the fault, and it occurs either as an *in situ* alteration product of olivine or glass, or disseminated in the rocks. Glass alteration is most notable in the Selatrað damage zone sample, which contains large (>50 μm) grain-shaped clusters of chlorite, while the most prominent example of olivine can be found in the Gøtugjógv damage zone sample (top left

363 in Figure 6C). This altered olivine grain is composed of a fine-grained mixture of chlorite,
364 illite, and saponite and displays the characteristic intracrystalline cracking of olivine.
365 Measured concentrations of smectites are relatively low in all samples (Figure 6A).
366 Mineral mapping only reveals significant concentrations of saponite in one sample, but, as
367 mentioned above, the texture in high magnification BSE micrographs shows the typical
368 platy and/or spongy texture of clay minerals with grain sizes ≤2 µm (Figure 5J).
369
370

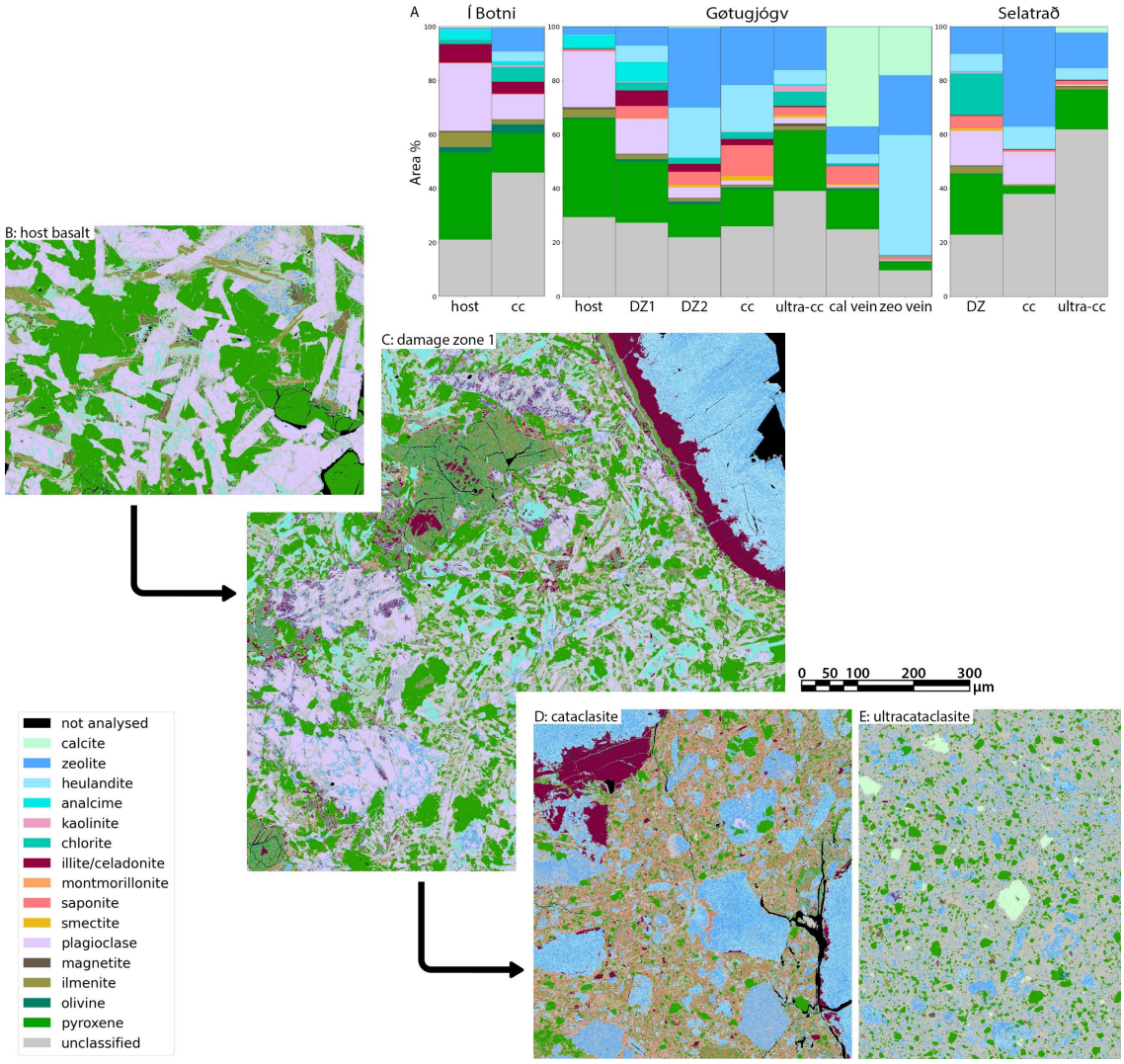

371

Figure 6. (A) SEM-EDS mineralogy and evolution from (B–E) host basalt to ultracataclasite in Gøtugjógv. (B) Replacement of plagioclase with analcime in assimilated host rock, (C) followed by analcime replacement with calcic heulandite, then (D) textural breakdown in cataclasite and complete zeolitisation and argillisation of the cataclastic matrix, and finally (E) intense comminution in ultracataclasite. The fine grain size of the latter inhibits reliable phase identification. Cc – cataclasite, DZ – damage zone, vein – fault vein.

4.3 Fault Rock Geochemistry

4.3.1 Whole Rock Major and Trace Element Composition (XRF)

The plagioclase-pyroxene to zeolite-smectite-pyroxene mineralogy of the samples is reflected in their major element whole rock composition, dominated by SiO_2, Al_2O_3, CaO, Fe_2O_3, and MgO, and minor amounts of Na_2O, K_2O, and TiO_2 (Table 1 & Figure 7).

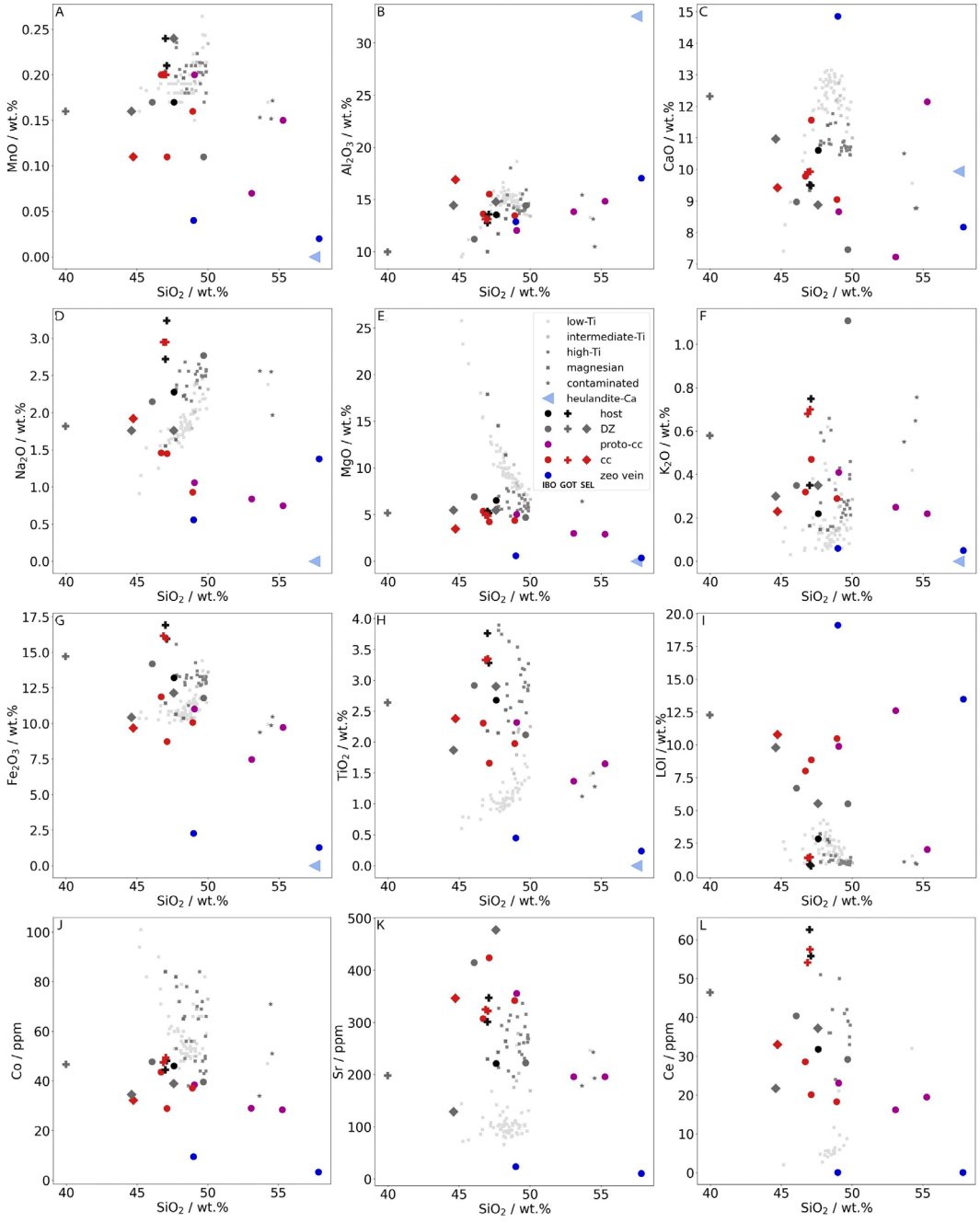

385

386 Figure 7. Harker plots showing basalt host and fault rock major and trace element
387 composition. Note general trend from undeformed high-Ti tholeiitic basalt towards
388 clinoptilolite-Ca composition in fault veins. The geochemical trends observable in our
389 samples are distinct from the trends in Faroe Islands basalts resulting from melt
390 fractionation. Geochemical data for different basalt types are taken from Holm et al. (2001)
391 and Søager and Holm (2011). Samples IBO1-1 and GOT12 are not shown on the plots
392 because of their high calcite content. DZ – damage zone, cc – cataclasite, IBO – Í Botni,
393 GOT – Gøtugjógv, SEL –Selatrað.
394

Whole rock chemical composition of our samples falls on a trend of decreasing major and trace element concentration towards higher SiO_2 concentrations, trending from high-Ti basalt composition towards an ideal clinoptilolite-Ca endmember (Figure 7). The only exceptions are Al_2O_3 and LOI, which correlate positively with SiO_2 (Figure 7B & I). The basalt and damage zone samples that were the furthest removed from the fault zone, as well as some cataclasite samples coincide with the composition reported for high-Ti basalts in the Faroe Islands (e.g. Holm et al., 2001; Søager and Holm, 2011), while (fault) veins are close to the clinoptilolite-Ca endmember, with compositions of breccias ranging in between. The trends observed in our samples are distinct from the element distribution observed in Faroe Island basalts which have SiO_2 contents between 45 wt.% and 50 wt.%. This is illustrated in Harker diagrams and element mobility plots (Figure 7 & Figure 11, respectively). The chemical composition remains largely unchanged throughout the fault zone, the only major excursions being samples with abundant calcite (IBO1-1 & GOT12) or zeolite cement (GOT23 & GOT5v). The Gøtugjógv samples display a weak trend from the host rock (GOT13) to increased Si and reduced Fe in fault core breccias (peaking around GOT20), and back to a primary composition in ultracataclasite (GOT26) (Table 1 & Figure 7). Due to the low number of samples from Í Botni and Selatrað, the following description will focus mainly on samples from Gøtugjógv. The patterns described there are reflected in the data from the other two fault zones.

The protolith samples selected as a reference for further analysis are the most pristine rocks that were accessible close to the fault outcrops, and fall within the typical basalt composition reported for the Faroe Islands (Figure 8). They are averaged Í Botni hanging wall and footwall host rock (samples IBOhwhost & IBOfwhost), Gøtugjógv hanging wall

418 host rock (GOT13, Figure 5A & C), and the relatively unaltered wall rock from a distal
419 damage zone fracture in Selatrað (SEL2, Figure 5B & D). Petrographic analysis and SEM-
420 EDS mineralogy (Figure 6) of the Í Botni host rock samples shows a fully preserved
421 basaltic assemblage with unaltered calcic plagioclase, pyroxene, glass, and opaques, but
422 olivine has been replaced with iddingsite. The Gøtugjógv and Selatrað samples show minor
423 plagioclase alteration along intracrystalline fractures, as well as partial glass breakdown
424 (Figure 5A–D).
425

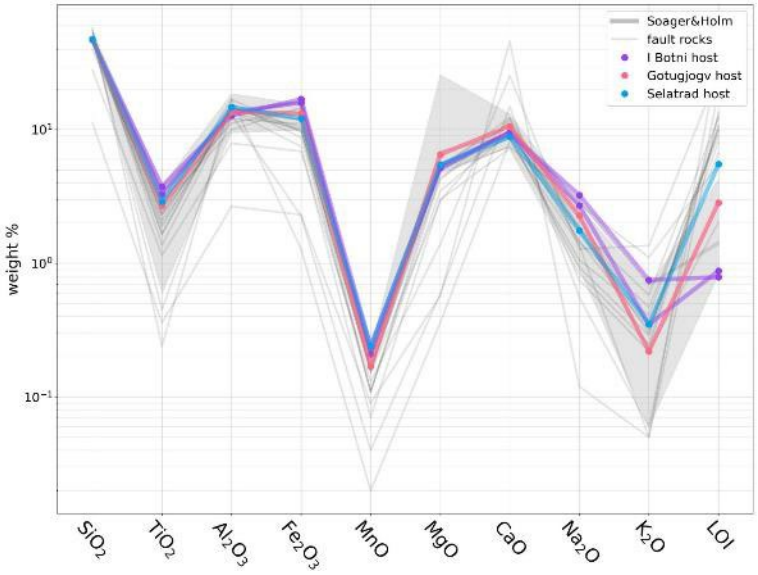

426

427 Figure 8. Major element composition of protolith sample used for each fault zone
428 compared to published data for basalts from the Faroe Islands (Søager and Holm, 2011)
429 and fault rock samples.
430

431 We assess element mobility in the faults comparing fault rock composition to their local
432 protolith using isocon diagrams (Figure 9) (Grant, 1986; Ague, 1991; Hippertt, 1998). They
433 reveal that Zr, and to a slightly lesser extend TiO_2, MgO, Cu and Zn remain immobile
434 during fault rock deformation (Figure 9). We therefore used Zr in the following as a

435 reference element to calculate global mass change (Figure 10) and element mobility
436 (Figure 11 & Figure 12). Global mass change (mass of the altered sample M^A versus mass
437 of protolith M^0) can be calculated via the concentration of the immobile element in the
438 altered sample C_i^A compared to the concentration of the immobile element in the protolith
439 C_i^0 using (Grant, 1986; Ague, 1991):

440 $$\frac{C_i^0}{C_i^A} = \frac{M^A}{M^0} \quad (1)$$

441

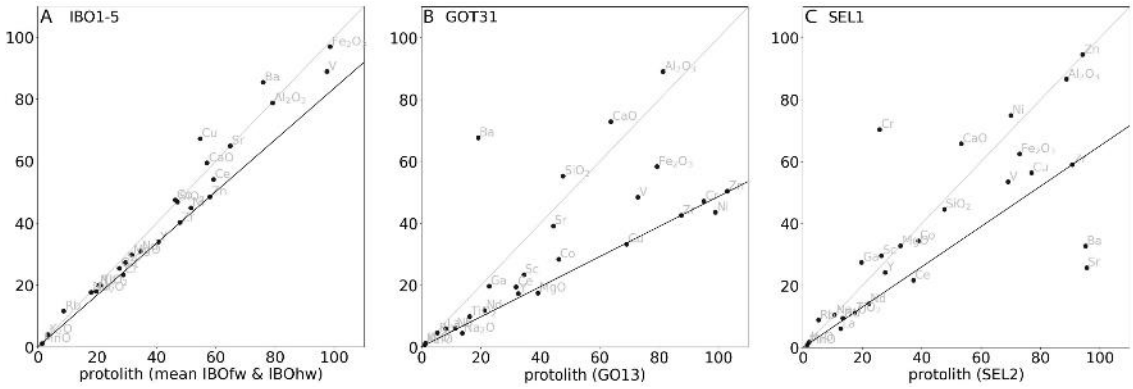

442

443 Figure 9. Representative isocon diagrams from each fault zone, plotting fault rock against
444 protolith compositions. The selected protolith samples are the most pristine rock that was
445 accessible at each fault zone. The black isocons connecting immobile elements plots below
446 the light grey constant mass reference line, indicating mass gain in all three samples.
447 Isocon diagrams for all analyzed samples can be found in the Appendix.
448
449 In Gøtugjógv, the relative mass change compared to host rock, records a mass loss (-7 %)
450 in the damage zone, 0.5 m away from the fault core (GOT34) compared to protolith, and
451 mass gains (ca. 23 %) in the damage zone directly in contact with the core (GOT21),
452 increasing to up to 105 % in cemented breccias (GOT20), and returning to 23 % in the
453 ultracataclasite sample (GOT26). For the fault veins, total mass gain ranges between 490 %
454 (GOT5v) and 1000 % (GOT23). Selatrað shows a similar pattern with mass gain of 53 % in

455 the ultracataclasite (SEL1), while Í Botni shows a relative mass change within ± 20 %,
456 where cement is absent, and up to 200 %, where cemented with calcite (IBO1-1) (Figure
457 10).
458

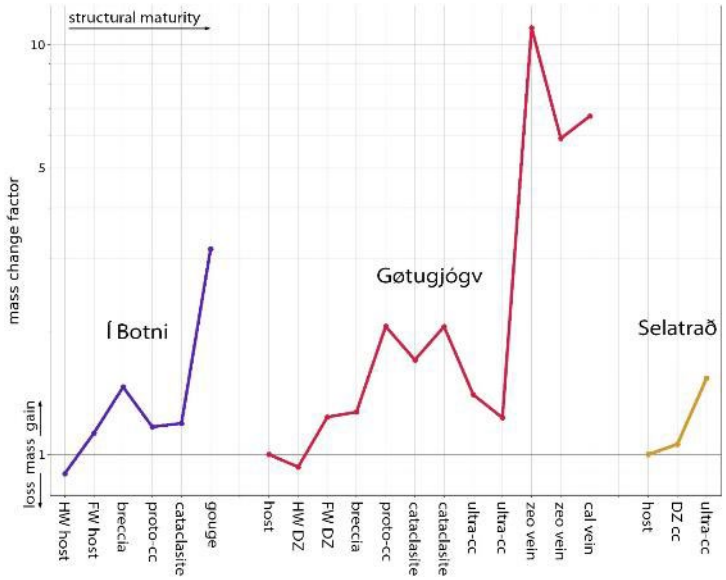

459

460 Figure 10. Global mass change compared to local protolith (M^A / M^0, Equ. 3.1). Protoliths
461 are mean IBO host, GOT13, and SEL2. Values <1 denote mass loss (e.g., leaching),
462 whereas values >1 denote mass gain (e.g., cementation).
463

464 Diagrams of element concentration plotted against immobile Zr from all samples show the
465 mobility of individual oxides/elements undistorted by the effect of global mass change
466 (Figure 11 & Figure 12). Immobile elements plot on the isocon connecting the origin to the
467 protolith. Samples that plot above the isocon have gained the relevant oxide (i.e., they are
468 enriched), whereas samples that plot below the isocon are depleted relative to the host rock.
469 The plots reveal dominantly fault internal redistribution of SiO_2, Al_2O_3, CaO, and LOI.
470 With the exception of the calcite-cemented breccia (not shown in plots), all samples fall on
471 a linear trend intersecting the isocon around the position of host rock composition. The

most distal damage zone rocks are relatively depleted of mobile elements, and zeolite veins are strongly enriched; cataclasites and breccias plot in between. K_2O shows increasing enrichment from veins, to cataclasite and breccia, and further to damage zone samples, relative to host rock, with the most significant enrichment in sample GOT21. K_2O is mainly contained in illite and celadonite, which are associated with amygdale linings and thus the primary porosity of the protolith. The host rock sample derives from a massive lava core with minimal porosity, and consequently low K_2O concentration. All other elements plot along their respective isocon, with normalized concentrations decreasing progressively from the damage zone through cataclasites and breccias to veins.

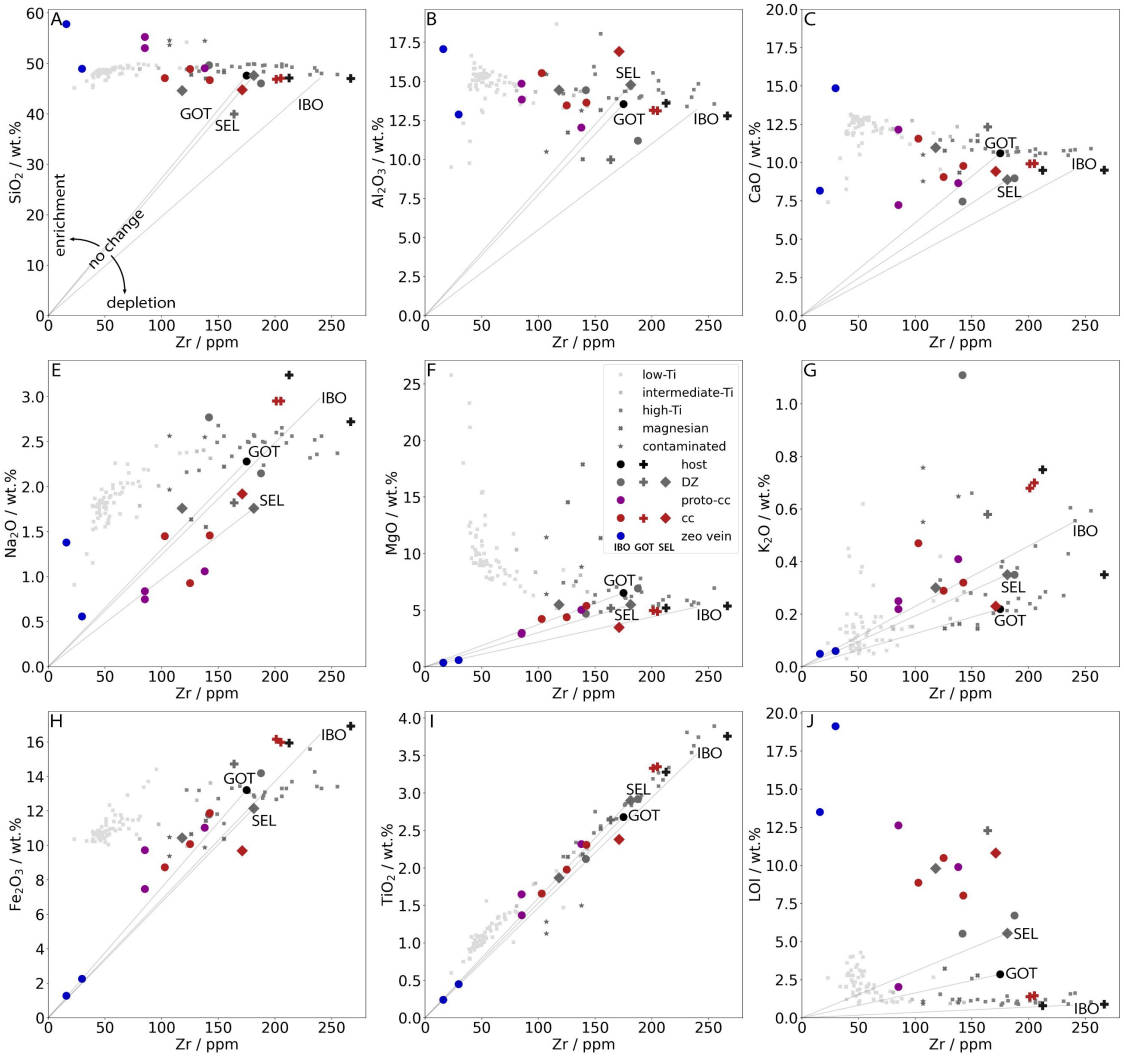

Figure 11. Element mobility plots showing ratios of major elements vs immobile Zr in all samples. Samples plotting on the isocon between the origin and the host rock have unaltered relative element concentrations, samples plotting below are depleted in the relevant element and samples plotting above are enriched. Only Si, Al, and Ca show significant deviations from the isocon, indicating that these elements are mobilized during fault rock alteration. They are depleted in the damage zone and enriched in the fault core and zeolite fault veins. Samples IBO1-1 and GOT12 are not shown on the plots because of their high calcite content. Geochemical data for different basalt types are taken from Holm et al. (2001) and Søager and Holm (2011). DZ – damage zone, cc – cataclasite, IBO – Í Botni, GOT – Gøtugjógv, SEL – Selatrað.

Trace element concentrations generally follow the same trend as the immobile Zr. The only exceptions are Ba and Sr, as well as in some cases Cr, Sc, V, and Ni (Figure 12). Elevated Ba/Zr ratios indicate Ba enrichment in the Gøtugjógv damage zone, especially in the hanging wall. In the more mineralized samples, such as breccias and veins, the absolute concentrations of Ba and Zr are reduced due to the addition of zeolite/calcite cements, but Ba/Zr ratios stay similar. A similar trend can be observed for Sr in Gøtugjógv. Í Botni fault rocks show only slightly elevated Sr, Sc, and Ni in the calcite cemented fault rock breccia. Similarly, calcite-dominated rocks from Gøtugjógv have high Cr, Sc, and V. In the Selatrað fault rocks, Ba and Sr are slightly depleted, and Cr and Sc are strongly enriched in the ultracataclasite. Ba and Sr (and perhaps Cr) correlate with Fe concentration, while V and Sc correlate with Ca. It should be noted that Ba concentration in the Gøtugjógv host rock is about half the concentration from the literature for Faroe Island basalts (Søager and Holm, 2011) as well as 1/3–1/5 of the concentrations in Í Botni and Selatrað, respectively.

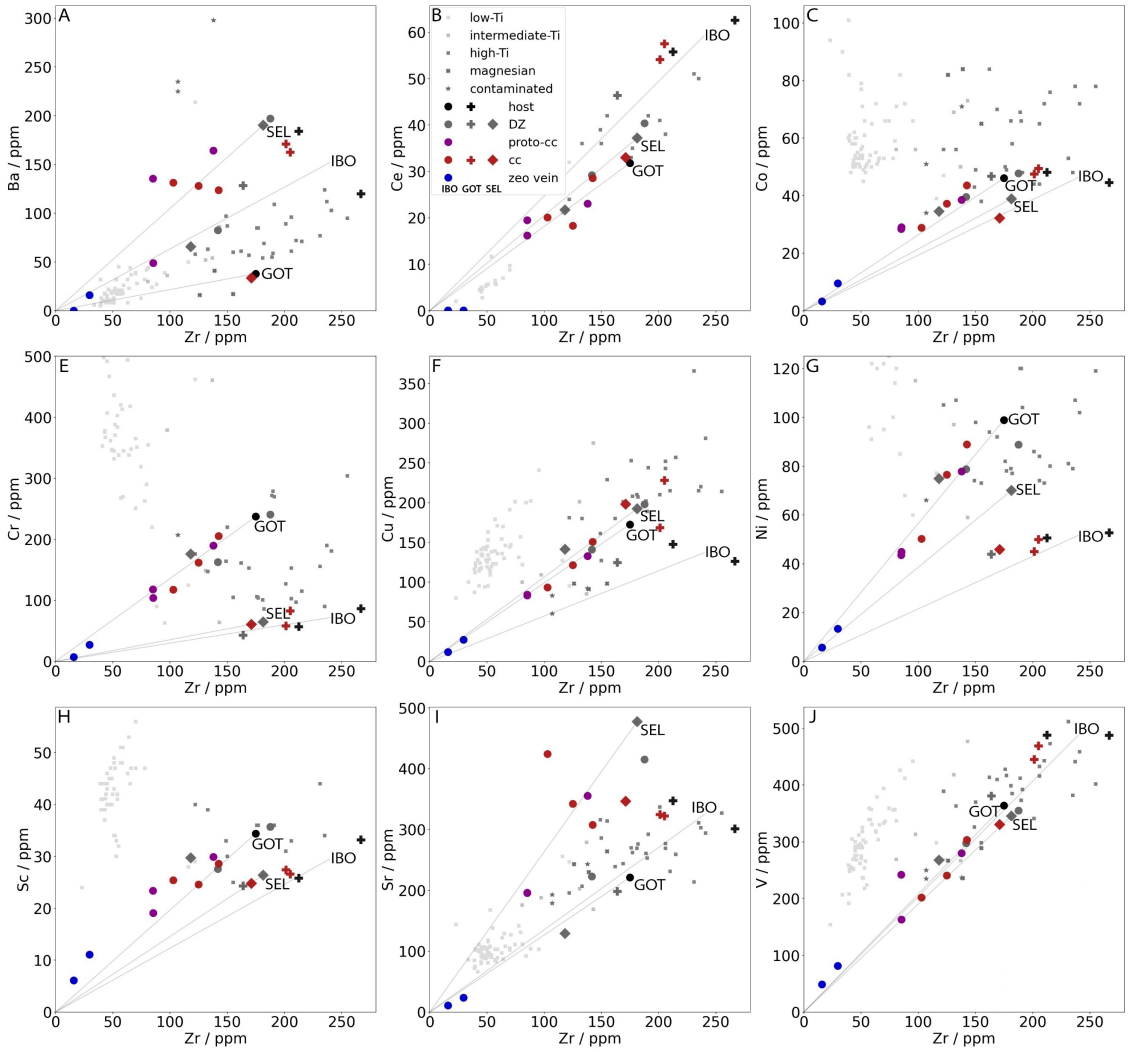

Figure 12. Element mobility plots of trace elements in all faults. Samples IBO1-1 and GOT12 are not shown on the plots because of their high calcite content. Geochemical data for different basalt types are taken from Holm et al. (2001) and Søager and Holm (2011). DZ – damage zone, cc – cataclasite, IBO – Í Botni, GOT – Gøtugjógv, SEL – Selatrað.

4.3.2 Element Distribution in Minerals (SEM-EDS)

All samples show almost complete olivine and glass breakdown and replacement by chlorite, mixed smectite, and unidentified phases. These secondary phases have high concentrations of Fe and Mg.

In the damage zone, Na is strongly concentrated in analcime at the expense of plagioclase, which is partially replaced. Ca concentration is not increased in the remnants of plagioclase compared to unaltered plagioclase, however anorthite/albite ratios increase from 1.1 in host rock to ≤3.1 in the fault core, consistent with preferential dissolution of albite. Only about 30–40 % of plagioclase is replaced by analcime. Besides plagioclase, Ca is concentrated in heulandite and other zeolite phases (excluding analcime), filling vesicles or replacing plagioclase closer to the core. Zeolites tend to have a higher Si and a lower Al concentration than plagioclase. The volcanic glass and secondary minerals filling interstitial space in between plagioclase and pyroxene grains (or remnants) have variable compositions, either similar to Fe-Ca-pyroxene or a Na-Ca-zeolite. Mg concentration in pyroxenes remains stable across the entire fault zone. However, Fe/Fe+Mg+Ca in pyroxene decreases by about 10 wt.% from host rock to cataclasite in Í Botni, and then another 10 wt.% to samples from Gøtugjógv and Selatrað, whereas the relative Ca concentration increases by only about 1 wt.%. The only other phases containing Mg are rare saponite and illite/celadonite, the latter also concentrating most of the K.

In the fault core, analcime is absent and Na is only abundant in remnant plagioclase. The remaining Na, as well as K, is contained in very low concentrations in zeolites and unidentified phases of the cataclasite matrix. Ca concentration is more homogeneous across the fault core compared to the damage zone or host rock, as it is relatively evenly distributed between zeolites, smectites, and unidentified phases, and abundant only in pyroxene and calcite cements. In fault core breccias, Fe is still chiefly contained in pyroxenes and ilmenite/magnetite, but also secondary phases from glass and olivine breakdown. In the cataclasite matrix, Fe concentration is consistently high, exceeding the

concentration in pyroxene. Si is abundant in zeolite grains of the (ultra-) cataclasites, whereas Al is more evenly distributed between zeolites, smectites, and unidentified phases. Ultracataclasites from Gøtugjógv and Selatrað, as well as the cataclasites from Í Botni, have a high concentration of unidentified matrix with no measurable Mg, low Si, but high Al, Ca, and Fe.

5 Interpretation & Discussion

5.1 Limitations of Automated Phase Identification using SEM-EDS

Although a powerful tool for rapid mineral identification and classification, automated phase identification based on EDS chemical analysis is subject to the same limitations as manual mineral identification in SEM spectroscopy. For example, minerals that share near-identical chemical compositions, such as Fe-Mg-illite and celadonite, are indistinguishable using this method despite being easily distinguished optically. This is prominently illustrated in the lining of amygdales (Figure 5G & Figure 6C). Furthermore, owing to the small grain size of some of the samples (e.g., cataclasites) and secondary phases, individual measurements (i.e., data points, or pixel) can reflect the superposed spectra of more than one phase contained in the interaction volume of the X-rays, measuring a few micrometers across. We refer to such measurements as a ‘mixel’ (a portmanteau for mixed pixel). These measurements are sometimes misclassified, but more often cannot be matched to one of the predefined mineral phases and remain unclassified. These limitations demand that the compositional ranges for mineral classification (i.e., the mineral recipe) be defined in a way that balances the proportion of measurements that can be classified (wider ranges) against the proportion of misclassified measurements (smaller ranges).

Automated phase identification in the host rock and damage zone generally agrees well with our petrographic observations. Plagioclase and pyroxene grain boundaries in mineral maps coincide with grain boundaries identified in BSE micrographs, whereas zeolites and clay minerals tend to be mapped only partially. In particular, the matrix composition in cataclasites tends to be poorly mapped (Figure 6A & E).

Despite chemical analysis by EDS being performed without calibration to a reference material, the resulting whole rock composition matches well with the whole rock composition measured by XRF (recalculated as element concentration assuming all Fe is Fe_2O_3) (Figure 13). Significant differences are notable for sample SEL3, which contains large amounts of zeolite, whose constituents are over-reported (by 1.1–2.7 wt.%) at the expense of Fe, Mg, and Ti (by 5.3 wt.%, 2.0 wt.%, and 1.3 wt.%, respectively) in EDS. Overall, Si tends to be over-reported, and O over- or under-reported in EDS compared to XRF. Concentrations of all other elements are generally within 1 wt.% difference between XRF and EDS. Notably, the EDS data is unreliable for elements with low concentrations (e.g., K and Ti) as the accuracy of around 1 wt.% equates to large relative errors (Figure 13). Reliability might be improved by increasing the analytical dwell times.

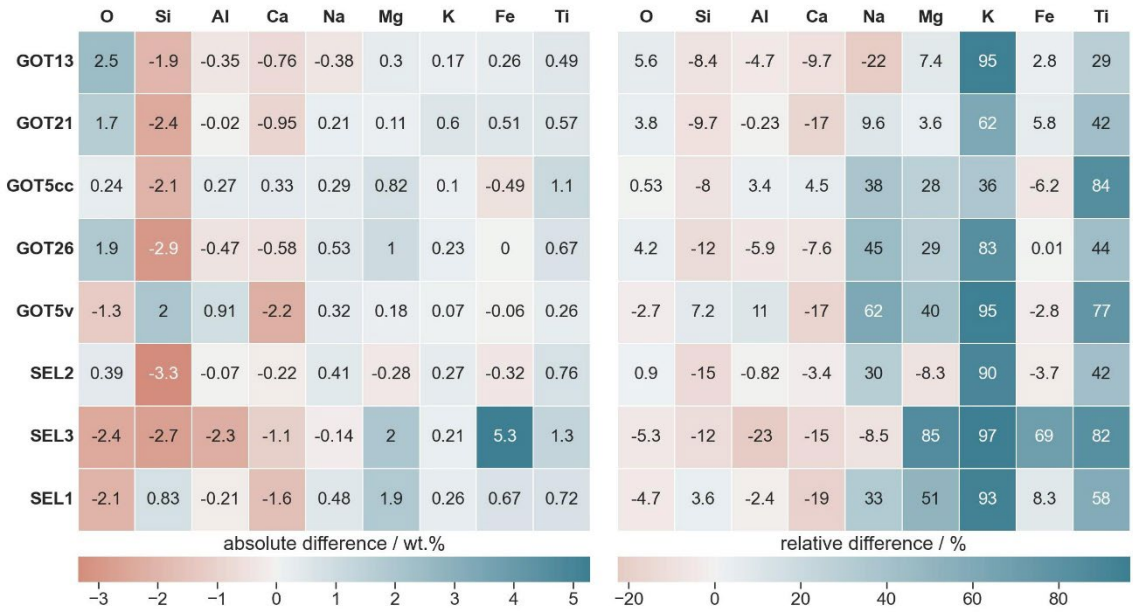

Figure 13. Difference between whole rock chemical composition measured by XRF (assuming full oxidation) and SEM-EDS. The composition from both methods was normalized to the sum of the elements considered here before calculating the difference $concentration_{XRF} - concentration_{EDS}$. Relative difference is normalised to the XRF data.

5.2 Mineralogical Composition and Evolution

Examination of undeformed host rocks indicates that the earliest phase of alteration affects olivine and volcanic glass (Figure 5A–C). These are typically the first phases to break down in a wide range of alteration conditions (Gislason and Eugster, 1987a; Frolova et al., 2014; Mattioli et al., 2016). In particular unaltered olivine is very rare in analyzed samples, including within protolith samples from outside the fault zones (Figure 5A), indicating that its breakdown might be diagenetic rather than related to faulting. Secondary mineral phases replacing olivine are classified as a mixture of pyroxene, saponite, and chlorite by automated phase classification (Figure 6C). Pyroxene is an unlikely alteration product, and more likely represents a mixed phase analysis (i.e., a mixel) and/or another secondary Fe-

595 Mg silicate, which has no Al but incorporated some Ca. Common alteration products of
596 olivine are iddingsite and clay minerals, such as celadonite and nontronite (Alt and
597 Honnorez, 1984; Mattioli et al., 2016). Volcanic glass and its alteration products are
598 commonly classified as chlorite, but show a distinct Mg gain and Si (+Al) loss in the
599 fibrous alteration rim compared to the massive core. Optical characteristics of the fibrous
600 rim closely resemble those of palagonite (Figure 5F), even though the chemical
601 composition does not match such a mixed smectite-zeolite phase. Considering the zeolitic
602 cores observed in pockets of volcanic glass in some host rock and distal damage zone
603 samples, and fibrous habits observed in host rock samples (Figure 5A), volcanic glass is at
604 least partially devitrified before deformation-related alteration sets in. The fibrous rims
605 might be chlorite as suggested by SEM-EDS mineralogy, however, the different
606 composition and optical characteristics of the green-brown cores indicate that this is
607 another cryptocrystalline Fe-Mg silicate with lower Fe and Mg, and higher Si content than
608 the surrounding chlorite. In other studies, volcanic glass is often found to be replaced by
609 aggregates of cryptocrystalline zeolites (Frolova et al., 2014), clays and Fe-oxy-hydroxides
610 (Alt and Honnorez, 1984; Mattioli et al., 2016) or a mixture of those (Ghiara et al., 1993).
611 Fault rocks representative of early damage concentration in the fault zones are associated
612 with a reduction in relative Fe concentration in pyroxenes, as seen in damage zone samples
613 from Í Botni, crossing from pigeonite to augite composition. The released Fe thus could
614 contribute to the extensive red staining of rocks from the damage zone and cataclasites
615 (Figure 5E–I), which we suggest primarily binds onto clay minerals. This is followed by *in*
616 *situ* plagioclase zeolitisation, first into analcime (incorporating only Na, and releasing Ca)
617 and then also other, more calcic (7–10 wt.% Ca, 1–3 wt.% Na) zeolites around fractures

and veins, where more abundant fluids promote element mobility (Figure 5D–H, Figure 6B–C). Alteration to analcime only affects about 30–40 % of plagioclase (Figure 6A–C), possibly limited by the availability of Na, which is strongly depleted in other zeolites replacing plagioclase. Further, unclassified secondary phases resulting from *in situ* glass devitrification are most likely smectite minerals, zeolites, and Fe-oxy-hydroxides (Hawkins, 1981; Gislason and Eugster, 1987a; Mattioli et al., 2016). The latter are visible in thin sections as opaques (Figure 5C) and probably the cause of the observed brown-red coloration (Figure 5E–I). The small grain size of these phases inhibits phase identification using SEM-EDS; however, more detailed, site-specific EDS analysis as well as bulk and micro X-ray diffraction might be able to unravel the composition of devitrification products, clays, and other very fine-grained phases (at a micrometer scale).

Fault rocks representing initial localization of deformation into a fault core, indicate that analcime and most of the remaining plagioclase are replaced by more calcic zeolites (Figure 6B–C). Similarly, coarse, idiomorphic zeolites identified dominantly as heulandite, are precipitated into voids, presumably from the pore fluid (Figure 5G & Figure 6C). The generally stable Na concentration in whole rock data seen in our samples (Figure 11E) implies that secondary zeolitisation locally scavenges Na, probably at the expense of plagioclase and older zeolites. Na concentration should be increased in samples with abundant zeolite if significant amounts were transported by the pore fluid, as is the case for Ca (Figure 11C).

Composition of the brown-red, fine-grained matrix in (ultra-) cataclasites, representative of fault core rocks, is more puzzling. Large areas could not be identified from their EDS spectra (Figure 6E), and the grain size is too small for identification by optical petrography

641 (Figure 5I–K). The abundant platy to spongy habit observed in SEM-BSE micrographs
642 (Figure 5J) suggests high abundances of clay minerals (Frolova et al., 2014; Mattioli et al.,
643 2016), mixed with the slightly coarser equant zeolite and pyroxene fragments. However,
644 average chemical composition of the matrix is 5 wt.% Fe, 12 wt.% Al, 22 wt.% Si, 10 wt.%
645 Ca, ≤2 wt.% Na, and no Mg, which cannot be reconciled with the mineral composition
646 suggested above. Assuming the measured Fe represents small amounts of magnetite/Fe-
647 oxy-hydroxide mixed with the main constituent phase, the remaining chemistry roughly
648 matches a non-specific zeolite composition with (in atoms per formula unit) 23 O, 13 Al,
649 7.3 Ca, and 1.9 Na, assuming 72 O in the oxide formula. In this case, the platy/spongy
650 textures we observed in SEM-BSE might have resulted from dissolution reactions, as
651 Gislason and Eugster (1987a, their Figure 1B) observed similar reaction textures in their
652 dissolution experiments of crystalline basalts, although at 10× higher scales.

653 5.3 Pore Fluids

654 The fault rocks described in this study show evidence of fluid-mediated alteration focused
655 around sites of elevated permeability such as veins and fractures. Unfortunately,
656 groundwater chemistry data is not available for the Faroe Islands (Eidesgaard et al., 2019).
657 We assume here that the present-day hydrologic system is comparable to those in Iceland
658 or East Greenland, which have a similar geology and geography. In both regions, low-
659 temperature geothermal springs (<150 °C) are fed by meteoric waters that is thought to
660 form convection zones in fracture and fissure swarms (Arnórsson, 1995b; Hjartarson and
661 Armannsson, 2010). Icelandic low-temperature waters (Table 2) are generally neutral to
662 slightly alkaline (pH 6.1–10.6) and carbonated (<4100 ppm, but generally between 15–
663 60 ppm CO_2), with cation concentrations generally low (<20 ppm) except for Na, which

664 typically reaches hundreds-of-ppm (Arnórsson and Barnes, 1983; Gislason and Eugster,
665 1987b; Arnórsson, 1995b; Aggarwal et al., 2000). The concentration range of dissolved
666 SiO_2 is similar to the concentration range of CO_2 (Gislason and Eugster, 1987b; Arnórsson,
667 1995b). High-temperature geothermal fluids (Table 2) have a similar cation concentrations,
668 but are slightly acidic and reducing, with H_2S generally ranging in the tens- to hundreds-of-
669 ppm (Gislason and Eugster, 1987b; Arnórsson, 1995a).
670 At the time of faulting, the Faroe Islands were exposed to a much hotter climate as they
671 were emplaced during the Paleocene-Eocene Thermal Maximum, with global temperatures
672 5–8 °C higher than present-day (McInerney and Wing, 2011). Groundwater chemistry in
673 the young Faroe Islands might therefore be more similar to present day Hawaii or the
674 Deccan Traps. Groundwater samples collected in a borehole on the summit of Kilauea
675 (Table 2) are slightly alkaline (pH ~8) and have higher cation concentrations than Icelandic
676 geothermal waters and similar concentration ranges for SiO_2 and carbonate (reported in
677 HCO_3) (Tilling and Jones, 1991; Hurwitz et al., 2003). They are thought to form through
678 mixing of meteoric groundwater and magmatic gas (Hurwitz et al., 2003). At the coast,
679 groundwater composition (Table 2) only marginally deviates from seawater, with
680 enrichment limited to SiO_2 (Thomas et al., 1996). In the Deccan Traps, groundwaters
681 (Table 2) have a similar acidity and HCO_3 concentration, while cation concentrations tend
682 to be on the lower end of the concentration spectrum from Kilauea (Kale et al., 2021).
683 We observe strong enrichment of Ba and Sr in the damage zone, compared to low
684 concentrations in the basalt host (Figure 12A & I). This suggests that pore fluids might be
685 of meteoric origin and percolated down through the highly fractured damage zone. Ba and
686 Sr would be mobilized during plagioclase and matrix breakdown and transported along the

687 fault during downward flow in the damage zone, until they are incorporated into secondary
688 phases such as clays and Fe-oxy-hydroxides (Das and Krishnaswami, 2006). Ba has been
689 found to accumulate in the matrix and, to a smaller degree, in plagioclase phenocrysts
690 (Philpotts and Schnetzler, 1970; Bindeman and Davis, 2000). Sr is thought to dissolve from
691 primary basalt phases, especially feldspar and volcanic glass, at shallow depth, and then
692 accumulate in zeolites of the heulandite-stilbite zone, resulting in a vertical gradient
693 (Neuhoff et al., 2000). Since Ba and Sr are precipitated in the damage zone, they are
694 depleted in cements of the fault core precipitating later-on. Alternative fluid sources would
695 be seawater or upwelling, hot geothermal fluids. Our data do not show increasing Na-
696 concentrations in altered rocks, which could be expected if they were reacting with fluids
697 similar to the seawater-derived groundwaters in Hawaii (Thomas et al., 1996). Hot
698 geothermal fluids in Iceland are reducing due to high H_2S concentrations (Arnórsson,
699 1995a). However, XRF analysis found virtually no SO_3 in our samples (Table 1) and the
700 red staining indicates oxidizing conditions in the fault zone.
701 Major element concentration in the fault zone only deviates significantly from host basalt
702 in zones that contain abundant mineral cements (Figure 7 & Figure 11). Even there, only
703 CaO, SiO_2, and Al_2O_3 are enriched, and LOI is similarly elevated. Element mobility
704 diagrams (Figure 11 & Figure 12) show that fault rocks consistently plot between two
705 endmember compositions: altered damage zone (e.g. GOT34) and pure zeolite (± calcite)
706 vein (e.g. GOT23), showing how cementation is the only significant chemical influence
707 after initial host rock alteration. Mineral cements are dominantly calcite and Ca-zeolite, in
708 the form of heulandite (Figure 5N–P & Figure 6A), hinting at the presence of a carbonated
709 fluid. As fault rocks from the low-displacement fault in Í Botni only contain calcite

cements (Figure 6A), and calcite is also the dominant cement in the fault-distal damage zone in Gøtugjógv and Selatrað, we assume that the pore fluid initially contains relatively high carbonate concentrations. Carbonated, low-temperature groundwaters are common in Iceland (Arnórsson and Barnes, 1983; Gislason and Eugster, 1987b; Arnórsson, 1995b; Aggarwal et al., 2000), which has a similar geological setting to the Faroe Islands. Zeolite precipitation would only be possible after significant dissolution of Si and Al during damage zone alteration. A likely source for these elements is volcanic glass, where we can observe a distinct Si and Al loss from the potentially unaltered cores to the fibrous secondary minerals in the rims. This is supported by studies indicating order-of-magnitude higher dissolution rates for basaltic glass compared to crystalline basalt or its mineral components (e.g. Gislason and Eugster, 1987a), and the onset of volcanic glass dissolution is accelerated in carbonated, alkaline fluids (Hawkins, 1981), like those found in Iceland. As Ca does not accumulate in remnant plagioclase during replacement with analcime, which only incorporates Na, it must be released into the fluid. The same reaction also produces Si and Al as by-products. Basaltic glass dissolution has also been proposed as a source for Ca, Al, and Si, triggering zeolite mineralisations, in oceanic basalts (Alt and Honnorez, 1984; D'Antonio and Kristensen, 2005) as well as altered basalts in Scotland (Triana et al., 2012).

As indicated by the element mobility diagrams (Figure 11), CaO, Si_2O, and Al_2O_3 are transported from the damage zone to the fault core, where they are sequestered in zeolite and calcite cements. The lack of evidence for any external chemical input other than CO_2 in the original fluid suggests that the faults may trap fluids internally. This is also supported by permeability measurements on basalt-derived fault rocks from the Faroe Islands, which

733 show a high potential for cross-fault sealing with low permeability zones between the host
734 rock and damage zone, and again between damage zone and fault core (Walker et al.,
735 2013a; 2013b). Leaching of a large volume of damage zone rocks should release enough
736 Ca, Si, and Al for the spatially limited cementation of the fault core (explored further in the
737 next section). Alternation between zeolite and calcite precipitation is probably linked to
738 evolving carbonate activity in the fluid (Zen, 1961; Neuhoff et al., 2000). Early calcite
739 precipitation in Í Botni and replacement of plagioclase with Na-zeolite (i.e., analcime) in
740 Gøtugjógv indicate an initially high carbonate activity, preventing the precipitation of
741 Ca-zeolites (Zen, 1961; Neuhoff et al., 2000). Parts of the damage zone that are assimilated
742 into the fault core become hydraulically isolated by the surrounding, impermeable
743 cataclasites, limiting fluid exchange and pressure equilibration. Carbonate activity would
744 be reduced progressively as plagioclase and volcanic glass alteration releases Ca, Si, and
745 Al into the fluid, and calcite is precipitated. As a result, conditions would become more
746 favorable for Ca-zeolite precipitation. However, as zeolite cementation removes significant
747 amounts of Ca, Si, and Al from the fluid, especially following hydrofracture, carbonate
748 activity would rise again, and the remaining porosity is filled with calcite. Ca-zeolites are
749 the dominant precipitate as long as its components are sufficiently concentrated in the fluid,
750 but through their depletion carbonate activity increases and eventually prevents further
751 zeolite precipitation. At this stage, calcite is deposited until one of its building blocks is
752 exhausted, leaving a pore fluid that is depleted in all mobile species. Another contributing
753 factor could be that zeolite precipitation tends to remove silica faster from the solution than
754 it is being released from volcanic glass (Hawkins, 1981).

As we see evidence for repeated alternation between calcite and zeolite cementation in the fault cores (Figure 5N–P), a mechanism controlling the phase that is precipitated is needed, as well as one that allows for replenishment of the solutes (i.e., Ca, Al, Si, CO_2) following a hydrofracture and cementation event. The transition from zeolite to calcite precipitation is probably controlled by increasing carbonate activity in the evolving fluid (Zen, 1961; Neuhoff et al., 2000), as outlined above. A likely mechanism for replenishing solutes is partial reassimilation of zeolites and calcite (and potentially other mineral phases) through pressure-solution during and/or following cataclastic creep. The thick layers of cataclasites around slip surfaces suggest that most displacement in the fault core is accommodated by cataclastic creep, which is often accompanied by pressure-solution (e.g. Hadizadeh, 1994; Gratier et al., 2014) of mobile phases such as calcite and zeolites. Several samples, such as Í Botni breccias and some cataclasite from Gøtugjógv and Selatrað show discontinuous and curved foliae defined by accumulation of clays and opaques and could be interpreted as pressure-solution seams (Figure 5E & L). High mobility of the generally immobile Al in the fault zones seems surprising at first, but can be easily explained in the light of the petrological evolution of the fault rocks. Initial mobilization occurs during metasomatic replacement of plagioclase with much more unstable analcime and Ca-zeolite. These zeolites are then repeatedly dissolved through pressure-solution and reprecipitated during episodic hydrofracture. Various degrees of zeolite dissolution in creeping cataclasites could potentially also explain the variable concentration of residual clays in the matrix of (ultra-) cataclasites. However, these compositional inconsistencies could also have arisen from local differences and variability in protolith composition (e.g., fault veins yielding more zeolite, and assimilated damage zone rocks yielding more clay). Processes for fluid

778 replenishment that lack a mechanism for cement dissolution, such as fluid influx from an
779 external source, would lead to a progressive dilatation of the fault core and the increasing
780 dilution of residual basalt alteration products by Ca, Si, and Al, at increasing
781 displacements, which is not supported by our data (Figure 10, Figure 11, Figure 12).
782 Finally, the lacking evidence for fluid replenishment in the fault cores implies that failures
783 or potential ruptures of the fault zone are limited to the fault core, and do not typically
784 breach the core–damage zone boundary, as this would result in fluid ingress from the
785 permeable damage zone. Hence, mature faults in basalts should present a stable,
786 hydrologically closed system and act as quasi-permanent barriers to cross-fault fluid flow.
787 Such a permeability structure is corroborated by permeability measurements of Faroese
788 fault rocks (Walker et al., 2013a; Walker et al., 2013b).

789 ### 5.4 Mass Balance

790 If the fault zone remains hydrologically sealed during its evolution, the gross budget of
791 solutes has to balance out across the sealed fluid cell in the fault zone. The mass change
792 factors of individual elements T_m, as plotted in the element mobility graphs (Figure 11),
793 can be used to calculate the volume of leached damage zone material necessary to balance
794 enrichment in the fault core.

795 $$T_m = \left(\frac{C_i^0}{C_i^A}\frac{C_j^A}{C_j^0}\right) - 1 \qquad (2)$$

796 Where C_i is the concentration of the immobile element and C_j is the concentration of the
797 mobile element in the altered fault rock (C^0) and protolith (C^A) (Grant, 1986; Ague, 1991).
798 Since we cannot appreciate the lateral extent of fluid cells from our data, we can only
799 calculate a balance across a one-dimensional section of the fault zone, in which we use the

thickness of each sampled subzone instead of volume. This way, we can estimate the necessary thickness of leached rock by comparing the sum of the mass change factor in each subzone weighted by the subzone's width (W_{zone}) from all subzones that gained the considered species (i.e., positive mass change factor), to all the subzones that lost the species (i.e., negative mass change factor).

$$\sum_{enriched} T_{m,zone} \times W_{zone} \; + \sum_{leached} T_{m,zone} \times W_{zone} \; = 0 \qquad (3)$$

In the Gøtugjógv fault zone, this suggests that SiO_2 mobilization in ca. 12 m of damage zone is required to balance the enrichment through zeolite mineralization in the core and near damage zone (Table 3). Similar calculations suggest that about 4 m and 11 m of damage zone could provide the Al_2O_3 and CaO required to balance their enrichment in the fault core (see Appendix for calculation). The true thickness for CaO is likely to be lower, as we have included a relatively pure, 5 cm wide calcite vein in our calculations to provide an upper bound, but calcite veins in the fault zones usually contain significant amounts of zeolite and clasts (Figure 3C), which reduces their Ca concentration. It should also be noted that the thicknesses we calculated are very rough estimates, since we assumed a homogeneous mass change factor for each subzone, but their heterogeneity is likely to resemble the microtextural complexity of fault rocks. Nevertheless, leaching of a 4–12 m wide damage zone is possible in Gøtugjógv, where the total width of the damage zone is around 13 m.

5.5 Depth of Faulting

Amygdales in the analyzed fault rocks are almost exclusively filled by a thin lining of celadonite and less abundant smectites, followed by coarse heulandite towards the center

(Figure 5G & Figure 6C), which is also the most common cement in the fault zone (Figure 6). Heulandite and clinoptilolite-Ca have been found to destabilize around the same temperature (ca. 450 °C and 450–550 °C) in laboratory experiments (Ghiara et al., 1999), which might suggest that clinoptilolite in our samples is stable in the same temperature range as heulandite. This would place the fault zones in the heulandite/stilbite stability zone, from 90–100 °C to 110–130 °C (Kristmannsdóttir and Tomasson, 1978; Jørgensen, 2006). Illitisation of smectite minerals, which is commonly used for temperature estimation (Pytte and Reynolds, 1989; Velde and Vasseur, 1992), is most likely inhibited by the low availability of K in the study area. Using these temperature ranges and geothermal gradients proposed by Jørgensen (2006), ranging from 56 °C/km in the Enni formation to 66 °C/km in the Beinisvørð Formation, combined with estimated timing of faulting (syn-volcanic for Í Botni, post-volcanic for Gøtugjógv and Selatrað; Walker et al., 2011) fault cements and amygdale fills would have precipitated at depths of 1.4–2.0 km in Í Botni and 1.5–2.1 km in Gøtugjógv and Selatrað. This is slightly deeper than expected from zeolite mapping performed by Jørgensen (2006), which would place Í Botni and Gøtugjógv in the shallower mesolite zone between 1.0 km and 1.5 km. Notably, our analysis did not reveal any mesolite in the samples, even though it is compositionally closer to plagioclase than analcime, which forms during the first stage of zeolitisation. Fault-parallel fluid migration could potentially modify the geothermal gradients within fault zones. Upward welling of hot hydrothermal fluids would result in an increased gradient, whereas downward percolation of meteoric water could reduce the gradient. In our case, the latter is more likely, and could therefore imply that the faults were active at slightly larger depth than suggested above.

5.6 Implications for Fault Evolution

The studied fault zones cut through plagioclase-pyroxene dominated basalts with minor, diagenetically altered olivine, and partially devitrified volcanic glass (Figure 5A–C, Figure 6B). We apply a space for time substitution for fault rock assemblages, to summarize observations into a conceptual fault zone evolution model (Figure 14).

In the incipient fault zone (or at the edge of the damage zone), damage accumulation increases permeability and fluid-rock ratios (Bamberg et al., 2022). Meteoric, carbonated, and slightly alkaline water percolates along the damage zone, where it catalyzes early metasomatic alteration. Initially, Na-rich plagioclase is replaced by analcime, and volcanic glass continues to break down into smectites, zeolites, and Fe-oxy-hydroxides (Figure 5C–H, Figure 6B–C). This releases Ca, Al, and Si into the fluid (Figure 11), and leads to chemical weakening of the rocks (Frolova et al., 2014). Carbonate activity is reduced in the evolving fluid through calcite precipitation and mineral dissolution, until Ca-zeolites become the dominant precipitate. The weakened rock localizes deformation into a principal slip zone, establishing a fault core where displacement is accommodated by cataclastic flow (Figure 2B, E–G, Figure 5I, Figure 6D–E). Comminution and the potential accumulation of smectites reduce permeability, compartmentalizing the fault zone. Since fluids are now trapped in the core, chemical exchange and pressure equalization with the damage zone are inhibited (Figure 11). Fluids become pressurized due to compaction, eventually triggering hydrofracture (Proctor et al., 2020) and rapid cementation of the fault core (Figure 3B–C, F, Figure 5M–P). Zeolite precipitation depletes dissolved Si, Al, and possibly Ca, increasing carbonate activity in the fluid, and the remaining voids are filled with coarse calcite (Figure 5N–P). Widespread cementation strengthens the core, forcing slip zone migration into a weaker domain (Bamberg et al., 2022). The abandoned slip zone

869 is reworked by cataclasis (Figure 3D–E) (Bamberg et al., 2022) while pressure-solution
870 dissolves some of the cements and replenishes solutes in the fluid. Comminution and
871 cement dissolution reset the stage for a next hydrofracture event, and the fault zone
872 continues to evolve through episodic cycles of cementation-strengthening and shear-
873 compaction (Bamberg et al., 2022) with the only significant mineralogic changes being
874 cement precipitation and dissolution.
875

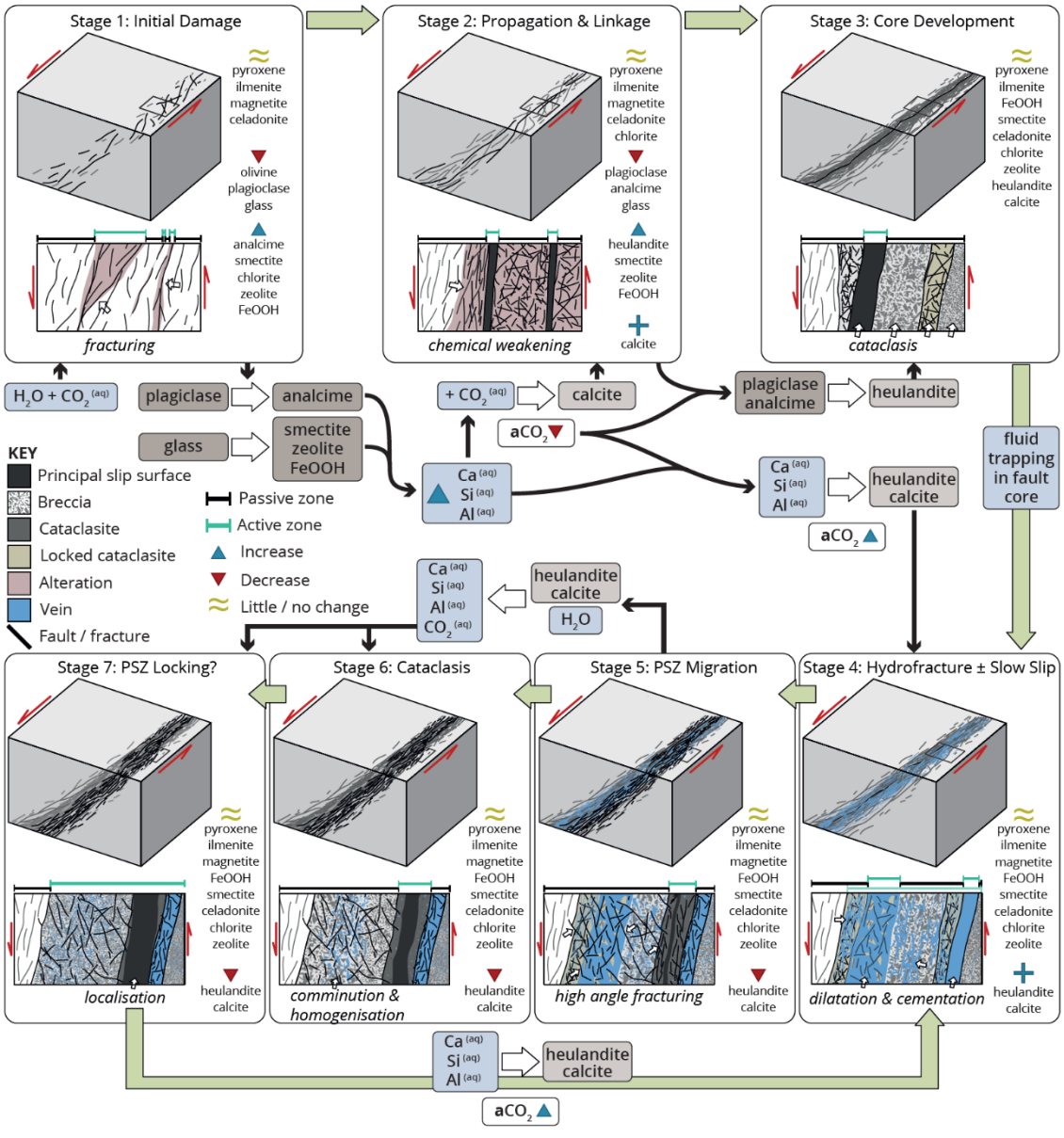

876

Figure 14. Conceptual model of fault evolution outlining the relative timing of petrologic alteration. Damage concentration in the early fault or damage zone increases permeability and thus fluid availability (Stage 1). Alteration of primary phases such as volcanic glass and plagioclase with carbonated waters releases Si, Al, and Ca into the fluid (Stage 1–2). As a result, carbonate activity in the evolving fluid drops and the primary precipitates change from analcime and calcite to Ca-zeolites such as heulandite (Stage 2–3). Low-permeability shear bands of comminuted and pervasively altered cataclasites trap fluids in the fault core, isolating the fault-internal fluid system (Stage 3). Ongoing shear increases internal fluid pressure, eventually triggering hydrofracture and rapid cementation with zeolites (Stage 4), which strengthen the core and force slip zone migration (Stage 5). Cataclastic creep in the new slip zone is accompanied by pressure-solution of calcite and zeolite cements, replenishing solutes in the fluid (Stage 6–7) and setting up the fault for a next pulse of hydrofracture and cementation (Stage 4). a CO_2 – CO_2 activity, (s) – solid, (aq) – aqueous.

6 Conclusions

Basalt-hosted fault zones in the Faroe Islands are sites of intense petrological alteration, featuring almost complete textural and mineralogical breakdown of the tholeiitic protolith. Olivine and volcanic glass alteration starts during diagenesis, but the primary phases are only completely replaced in damage zones breccias, where damage concentration increases fluid-rock ratios. Olivine is replaced by smectite, chlorite, and an unknown Fe-Mg silicate that can incorporate some Ca. Volcanic glass is replaced by aggregates of zeolite, smectite, and Fe-oxy-hydroxides. In the vicinity of the fault core, zeolites replace plagioclase. Zeolitisation progresses through two stages. First, Na-rich plagioclase is replaced by analcime, after which Ca-zeolites replace the remaining anorthite-dominated plagioclase and analcime. Only pyroxene and ilmenite/magnetite remain relatively unaltered. In the fault core, secondary phases, pyroxene and ilmenite/magnetite are mechanically mixed through cataclasis. Chemical mobility is limited to alternating heulandite and calcite precipitation and dissolution; the latter probably by pressure-solution during cataclastic creep in the core. The only mobile species are Ca, Si, Al, and CO_2. Carbonate is most likely

907 added through meteoric waters percolating through the damage zone. The fault cores
908 appear to be hydrologically sealed, inhibiting chemical exchange or fluid-pressure
909 equilibration with the damage zone and host rock.

910 **Acknowledgements**

911 We thank Tom Knott and Leon Hicks for their technical support on the SEM, and Lin
912 Marvin-Dorland for her help during XRF analysis. We also wish to thank Catriona
913 Menzies, David Holwell, and Jeremy Rushton for valuable discussions that greatly
914 improved this manuscript.

915 **Data Availability Statement**

916 The geochemical data (XRF raw data and reference analyses) and SEM-BSE and EDS
917 maps (incl. mineral maps, element concentration heat maps, and tabulated chemical
918 composition of each raster point) of the samples are available in the Open Science
919 Framework repository Bamberg, B. (2023, June 28). Basaltic Fault Rock Petrology.
920 Retrieved from osf.io/r3skf.

921 Table 1. Bulk rock composition (major elements) of selected fault rock samples in weight
922 percent. Raw data in data repository (Bamberg, 2023). Cc – cataclasite, cal – calcite,
923 DZ – damage zone, FW – foot wall, HW – hanging wall, LLD – lower limit of detection,
924 RSD – relative standard deviation, vein – fault vein, zeo – zeolite.
925

Sample	Rock Type	SiO_2	TiO_2	Al_2O_3	Fe_2O_3	MnO	MgO	CaO	Na_2O	K_2O	P_2O_5	SO_3	LOI
GOT13	**host**	47.60	2.68	13.54	13.21	0.17	6.52	10.61	2.28	0.22	0.22	0.10	2.85
GOT34	**HW DZ**	46.06	2.92	11.21	14.19	0.17	6.92	8.97	2.15	0.35	0.24	0.10	6.71
GOT21	**FW DZ**	49.68	2.12	14.43	11.79	0.11	4.71	7.46	2.77	1.11	0.20	0.10	5.52
GOT22	**breccia**	49.04	2.32	12.05	11.03	0.20	5.04	8.66	1.06	0.41	0.20	0.10	9.90
GOT31	**proto-cc**	55.27	1.65	14.85	9.73	0.15	2.92	12.15	0.75	0.22	0.17	0.10	2.03
GOT33	**cc**	47.11	1.66	15.53	8.73	0.11	4.24	11.57	1.45	0.47	0.16	0.10	8.87
GOT20	**cc**	53.06	1.37	13.84	7.48	0.07	3.01	7.23	0.84	0.25	0.12	0.10	12.62
GOT5cc	**ultra-cc**	48.91	1.98	13.47	10.08	0.16	4.38	9.05	0.93	0.29	0.17	0.10	10.49
GOT26	**ultra-cc**	46.69	2.31	13.64	11.88	0.20	5.39	9.79	1.46	0.32	0.20	0.10	8.03
GOT23	**zeo vein**	57.82	0.24	17.06	1.28	0.02	0.36	8.17	1.38	0.05	0.02	0.10	13.50
GOT5v	**zeo vein**	48.98	0.45	12.89	2.27	0.04	0.59	14.86	0.56	0.06	0.06	0.10	19.14
GOT12	**cal vein**	11.29	0.36	2.67	2.31	0.09	0.57	45.94	0.12	0.05	0.05	0.10	36.44
IBOhwhost	**HW host**	47.00	3.76	12.78	16.92	0.24	5.36	9.51	2.72	0.35	0.38	0.10	0.88
IBOfwhost	**FW host**	47.09	3.28	13.59	15.94	0.21	5.18	9.49	3.24	0.75	0.33	0.10	0.79
IBO1-4	**breccia**	39.97	2.64	9.98	14.72	0.16	5.16	12.32	1.82	0.58	0.26	0.10	12.28
IBO1-3	**proto-cc**	47.03	3.35	13.11	15.98	0.20	4.87	9.93	2.95	0.70	0.33	0.10	1.45
IBO1-1	**cc**	28.03	1.15	7.92	6.89	0.13	1.39	25.27	1.28	1.36	0.08	0.02	26.47
IBO1-5	**gouge**	46.86	3.33	13.14	16.16	0.20	4.96	9.91	2.95	0.68	0.33	0.10	1.39
SEL2	**host**	47.59	2.90	14.78	12.15	0.24	5.47	8.88	1.76	0.35	0.24	0.10	5.54
SEL3	**DZ cc**	44.74	2.38	16.91	9.68	0.11	3.48	9.42	1.92	0.23	0.22	0.10	10.80
SEL1	**ultra-cc**	44.61	1.87	14.44	10.43	0.16	5.48	10.97	1.76	0.30	0.17	0.01	9.80
LLD		0.40	0.01	0.28	0.02	0.01	0.13	0.05	0.17	0.01	0.02	0.08	
RSD / %		0.6	0.4	1.5	0.3	49.4	0.3	0.3	3.2	1.5	2.0	48.3	

926

927

928
929
930
931

Table 2. Fluid composition in Iceland, Hawaii, and the Deccan Traps. All concentrations are in ppm.

932

		temp. / °C	pH	HCO_3	CO_2	SiO_2	Ca	Na	Mg	K
Iceland										
Snaefellsnes cold water springs	*Arnórsson & Barnes, 1983*	4-6	4.5-6.2		616-4100	5-77	2-256	5-660	1-178	0-27
NE Iceland spring water	*Gislason & Eugster, 1987b*	2-34	7.7-10.2		18-85	12-93	1-74	89-193	0-22	0-10
High-temp. geothermal waters	*Arnórsson, 1995a*	181-340	5.3-7.2		154-15534	271-664	0-1467	76-9594	0-1	6-1480
Low-temp. geothermal waters	*Arnórsson, 1995b*	7-147	6.1-10.6		1.7-1358	21-182	1-560	9-486	0-21	0-37
SW Iceland geothermal	*Aggarwal et al., 2000*	7-92	6.2-10.7		11-1101					
Hawaii										
Kilauea summit borehole (NSF)	*Tilling & Jones, 1991*		7.6-8.7	150-1080	20-35	67-180	36-106	214-769	22-110	43-142
Hawaii flank borehole (KP-1)	*Thomas et al., 1996*		7.5-7.9	61-140		9-39	76-478	1740-11700	224-1320	67-398
Kilauea summit borehole (NSF)	*Hurwitz et al., 2003*	73-92	6.7-8.7			107-173	77-162	548-838	366-737	151-245
Deccan Traps										
Jalna groundwater	*Kale et al., 2021*	21-32	7.0-9.0	182-970			5-54	34-261	2-46	0-21

Table 3. Mass balance calculation for SiO_2 across a section of the Gøtugjógv fault zone using equation 3.3. SiO_2 is leached from the far damage zone and enriched in the near damage zone and fault core. Summing the mass change factors ($\boldsymbol{T_{SiO_2}}$) in the enriched subzones weighted by the subzones' width ($\boldsymbol{W}$) gives the total amount of SiO_2 that has been mobilized ($\boldsymbol{M_{SiO_2}}$; left-hand table). Dividing this by the mass change factor in the depleted far damage zone yields the width of leached damage zone required to balance SiO_2 redistribution (11.97 m ; right-hand table). Cal – calcite, DZ – damage zone, zeo – zeolite.

SiO_2 enrichment in

structure	**sample**	$\boldsymbol{T_{SiO_2} \times W / m}$		$\boldsymbol{= M_{SiO_2}}$
near DZ	GOT21	0.29	0.30	0.09
breccia	GOT22	0.31	1.50	0.46
protocataclasite	GOT31	1.29	0.10	0.13
cataclasite	GOT33	1.39	0.05	0.07
cataclasite	GOT5cc	0.44	0.30	0.13
ultracataclasite	GOT26	0.21	0.05	0.01
zeo vein	GO5Tv	5.08	0.05	0.25
cal vein	GOT12	0.59	0.05	0.03
Total			2.40	**1.17**

→

SiO_2 leaching from

structure	**sample**	**Total $\boldsymbol{M_{SiO_2} / T_{SiO_2}}$**		$\boldsymbol{= W / m}$
far DZ	GOT34	**1.17**	-0.10	**-11.97**

Appendix

SEM-EDS Mineralogy

Table A-1: Hierarchical list of phase composition used for automated phase classification. The lower bound is indicated by a minus (-) and upper bound by a plus (+) for each element or element ratio. All concentrations are in %.

	Al-	Al+	O-	O+	K-	K+	Si-	Si+	Na-	Na+	Mg-	Mg+	Fe-	Fe+	Ca-	Ca+	Ti-	Ti+	Si/Al-	Si/Al+	(Al+Si)/(Na+Ca)-	(Al+Si)/(Na+Ca)+	(Mg+Ca+Fe)/Si-	(Mg+Ca+Fe)/Si+
Kaolinite	12	40	15	65	0	0.001	15	50	0	1	0	1	0	1	0	1								
Calcite	0	1	33	63			0	1			0	6	0	7	24	70								
Ilmenite	0	10	20	50			0	20					20	55			15	40						
Magnetite	0	10	10	50			0	20					55	80			0	20						
Illite	0	24	30	55	3	12	17	37			0	8	0	20										
Chlorite	1	15	30	60	0	1.9	12	40	0	1	0	25	4	25	0	1								
Pyroxene	0	3	15	50	0	0.01	15	35	0	10	3	24	0.5	30	0	35								1.5
Olivine	0	3	15	50			10	30	0	1	0	40	0	60	0	1							1.5	
Analcime	10	20	30	60			20	40	5	15					0	1								
Montmoril.	8	15	20	65	0	1	15	50	0	6	1	5	0	1	0	12			2					
Saponite	5	10	30	50			15	32	0	1	3	25	8	20	0	8								
Plagioclase	8	22	35	45			18	34	1	11	0	0.01	0	0.01	6	17	0	0.01		4		4.7		
Heulandite	6	13	35	55			27	40	0	1	0	1	0	1	4	12			2.5		4.7	10		
Thomsonite	1	13	20	60			20	40	0	5			0	1	4	15			0.5	1.5		3.5		
Beidellite	10	22	30	52	0	1	15	50	0	7	0	5	0	1	2	14				2	10			
Smectite	6	30	20	65	0	1	15	50	0	5	0	25	1	25	0.01	4								
Zeolite	1	13	20	60			20	40	0	5	0	1	0	1	4	15			1					

954 X-ray Fluorescence

Sample	Rock Type	Ba	Ce	Co	Cr	Cu	Ga	La	Nb	Nd	Ni	Rb	Sc	Sr	V	Y	Zn	Zr
GOT13	host	38.0	31.8	46.1	237.5	172.6	22.7	8.1	11.3	21.2	98.9	5.3	34.4	221.4	364.1	32.5	102.9	174.9
GOT34	HW DZ	197.2	40.4	47.8	240.8	197.9	17.9	11.0	12.1	25.7	88.8	5.3	35.7	415.1	355.2	34.2	109.3	187.6
GOT21	FW DZ	82.6	29.2	39.6	162.6	141.0	16.4	11.0	9.1	18.4	78.8	22.0	27.6	222.9	297.9	26.7	83.8	141.7
GOT22	breccia	164.3	23.1	38.5	189.7	132.8	17.1	9.4	9.4	15.2	77.8	7.3	29.9	355.6	280.2	24.1	78.1	137.8
GOT31	proto-cc	135.4	19.5	28.4	118.0	83.3	19.7	6.0	6.2	11.9	43.6	4.6	23.4	196.0	242.2	17.3	50.4	85.1
GOT33	cc	131.4	20.1	28.9	117.6	93.3	29.8	10.4	7.1	16.9	50.2	8.7	25.4	424.3	201.9	19.6	59.9	102.8
GOT20	cc	48.9	16.2	29.0	104.1	84.0	14.3	4.4	6.1	11.3	44.9	5.3	19.1	196.1	162.9	16.4	52.9	85.2
GOT5cc	ultra-cc	128.2	18.3	37.2	161.9	121.3	19.2	4.5	8.3	14.4	76.5	4.7	24.6	342.3	240.9	21.9	72.8	124.9
GOT26	ultra-cc	123.6	28.6	43.6	205.5	150.6	23.0	9.6	9.7	20.1	88.9	5.6	28.6	307.7	303.4	26.6	85.2	142.3
GOT23	zeo vein	0.1	0.1	3.3	7.1	11.7	4.6	0.1	2.3	4.1	5.7	2.7	6.1	10.8	48.6	2.8	8.6	15.9
GOT5v	zeo vein	16.1	0.1	9.5	27.2	27.4	5.0	3.1	3.4	4.9	13.4	3.3	11.1	23.7	81.6	6.1	17.3	29.6
GOT12	cal vein	54.8	0.1	5.0	140.6	20.5	7.3	0.1	3.6	5.0	22.3	3.3	46.7	28.8	1333.2	10.0	21.7	26.1
IBOhwhost	HW host	119.8	62.6	44.5	86.6	126.1	27.5	21.7	19.7	38.1	52.7	4.8	33.2	301.2	487.4	47.9	124.7	266.7
IBOfwhost	FW host	184.0	55.8	48.1	56.9	147.5	27.4	17.5	21.0	31.0	50.5	12.5	25.8	347.2	487.8	33.3	107.2	212.5
IBO1-4	breccia	128.3	46.4	46.7	42.8	124.4	17.8	14.7	16.7	24.2	43.9	10.0	24.3	198.1	380.8	25.2	79.6	163.9
IBO1-3	proto-cc	162.6	57.5	49.4	82.6	228.1	25.7	17.9	20.2	30.2	49.9	12.0	26.6	322.1	468.9	33.7	101.4	205.1
IBO1-1	cc	62.8	17.6	21.5	23.1	95.9	13.9	7.7	7.3	8.3	34.1	32.4	29.6	205.1	139.6	14.3	38.2	75.4
IBO1-5	gouge	171.0	54.1	47.5	58.3	168.2	25.5	18.0	20.0	31.0	45.0	11.7	27.4	324.8	445.1	34.0	97.1	201.2
SEL2	host	190.2	37.2	38.9	64.5	192.4	19.7	12.7	13.4	22.1	70.0	5.2	26.4	477.6	345.2	27.7	94.2	181.3
SEL3	DZ cc	33.5	33.0	32.2	60.7	198.0	38.8	8.8	12.8	22.8	45.8	3.0	24.8	346.3	330.6	28.7	81.0	171.1
SEL1	ultra-cc	65.6	21.7	34.5	176.0	141.1	27.5	6.1	9.5	14.1	74.9	8.9	29.7	129.1	267.8	24.3	94.6	118.1
RSD / %		2.6	8.2	3.5	1.1	1.6	2.7	12.3	1.6	6.3	1.3	2.2	3.1	0.2	0.5	1.4	1.0	1.3

Table A-2: Bulk rock composition (trace elements) of selected fault rock samples in weight percent.
Cc – cataclasite, cal – calcite, DZ – damage zone, FW – foot wall, HW – hanging wall, RSD – relative standard deviation, vein – fault vein, zeo – zeolite.

Table A-3: Absolute (ASD) and relative standard deviation (RSD) for major element analysis in XRF determined on Whin Sill dolerite (Govindaraju, 1994). Concentrations in weight percent.

	SiO_2	TiO_2	Al_2O_3	Fe_2O_3	MnO	MgO	CaO	Na_2O	K_2O	P_2O_5	SO_3	Total
Reference value	***51.31***	***2.54***	***14.04***	***13.51***	***0.18***	***5.31***	***8.87***	***3.10***	***1.36***	***0.30***	***0.00***	
27/04/2017	51.37	2.51	13.70	13.56	0.17	5.35	8.74	2.79	1.31	0.30	0.06	99.89
17/05/2017	51.64	2.52	13.80	13.56	0.17	5.36	8.74	2.77	1.31	0.30	0.07	100.24
30/05/2017	51.42	2.52	13.80	13.57	0.17	5.38	8.76	2.78	1.31	0.30	0.07	100.08
06/06/2017	51.49	2.51	13.80	13.59	0.17	5.35	8.75	2.78	1.32	0.30	0.07	100.12
28/06/2017	51.42	2.51	13.74	13.56	0.17	5.37	8.76	2.77	1.31	0.30	0.07	99.98
06/07/2017	51.36	2.51	13.74	13.56	0.17	5.34	8.76	2.79	1.31	0.30	0.07	99.91
25/09/2017	51.69	2.53	13.96	13.56	0.17	5.35	8.82	2.81	1.32	0.31	0.17	100.69
13/07/2017	51.57	2.53	13.98	13.58	0.17	5.41	8.72	2.85	1.32	0.31	0.16	100.61
19/07/2017	51.66	2.52	13.91	13.57	0.17	5.37	8.79	2.82	1.32	0.31	0.16	100.60
01/08/2017	52.00	2.52	14.00	13.55	0.17	5.38	8.80	2.84	1.32	0.31	0.16	101.05
08/08/2017	51.53	2.52	13.98	13.46	0.17	5.36	8.79	2.82	1.32	0.31	0.17	100.42
09/08/2017	51.53	2.52	13.98	13.46	0.17	5.36	8.79	2.82	1.32	0.31	0.17	100.42
14/08/2017	51.89	2.52	13.94	13.55	0.17	5.38	8.78	2.84	1.33	0.31	0.16	100.86
08/10/2019	51.37	2.50	13.83	13.54	0.17	5.33	8.78	2.82	1.32	0.32	0.15	100.14
18/12/2019	51.50	2.50	13.77	13.53	0.17	5.32	8.79	2.90	1.33	0.32	0.14	100.27
12/02/2020	51.33	2.49	13.73	13.54	0.18	5.42	8.76	2.82	1.32	0.31	0.15	100.06
14/08/2020	52.17	2.51	14.27	13.45	0.17	5.26	8.77	2.86	1.32	0.32	0.15	101.26
ASD (wt.%)	***0.3***	***0.0***	***0.2***	***0.0***	***0.0***	***0.0***	***0.0***	***0.0***	***0.0***	***0.0***	***0.0***	
RSD (%)	***0.5***	***0.4***	***1.1***	***0.3***	***1.0***	***0.7***	***0.3***	***1.3***	***0.6***	***2.0***	***37.5***	

Table A-4: Blank analysis of Li-tetraborate flux indicating the lower limits of detection (=average + 3ASD).

	SiO_2	TiO_2	Al_2O_3	Fe_2O_3	MnO	MgO	CaO	Na_2O	K_2O	P_2O_5	SO_3	Total
27/04/2017	0.05	0.00	0.16	0.02	0.00	0.10	0.02	0.10	0.00	0.00	0.01	0.47
17/05/2017	0.06	0.00	0.17	0.02	0.00	0.10	0.02	0.11	0.00	0.00	0.02	0.51
30/05/2017	0.06	0.00	0.16	0.02	0.00	0.10	0.02	0.11	0.00	0.00	0.01	0.51
06/06/2017	0.07	0.00	0.17	0.02	0.00	0.10	0.02	0.10	0.00	0.00	0.02	0.51
28/06/2017	0.06	0.00	0.16	0.02	0.00	0.10	0.02	0.11	0.00	0.00	0.02	0.51
06/07/2017	0.08	0.00	0.17	0.02	0.00	0.10	0.02	0.11	0.00	0.00	0.02	0.53
25/09/2017	0.27	0.01	0.25	0.02	0.00	0.12	0.04	0.14	0.00	0.01	0.05	0.91
13/07/2017	0.26	0.01	0.25	0.02	0.00	0.12	0.04	0.13	0.00	0.01	0.05	0.88
19/07/2017	0.22	0.01	0.23	0.02	0.00	0.12	0.03	0.13	0.00	0.01	0.04	0.80
01/08/2017	0.22	0.00	0.24	0.02	0.00	0.12	0.03	0.13	0.00	0.01	0.04	0.82
08/08/2017	0.22	0.01	0.24	0.02	0.00	0.12	0.03	0.13	0.00	0.01	0.04	0.82
09/08/2017	0.22	0.01	0.24	0.02	0.00	0.12	0.03	0.13	0.00	0.01	0.04	0.82
14/08/2017	0.23	0.01	0.23	0.02	0.00	0.12	0.03	0.13	0.00	0.01	0.04	0.82
08/10/2019	0.24	0.01	0.22	0.02	0.00	0.12	0.03	0.15	0.00	0.01	0.05	0.85
18/12/2019	0.00	0.00	0.04	0.02	0.00	0.08	0.02	0.14	0.01	0.03	0.07	0.41
12/02/2020	0.11	0.01	0.08	0.02	0.00	0.08	0.02	0.15	0.01	0.03	0.08	0.58
14/08/2020	0.02	0.01	0.05	0.02	0.00	0.08	0.02	0.15	0.01	0.03	0.08	0.47
Average	***0.13***	***0.01***	***0.17***	***0.02***	***0.00***	***0.10***	***0.03***	***0.13***	***0.00***	***0.01***	***0.04***	
ASD	***0.1***	***0.0***	***0.0***	***0.0***	***0.0***	***0.0***	***0.0***	***0.0***	***0.0***	***0.0***	***0.0***	
LLD	***0.400***	***0.010***	***0.283***	***0.024***	***0.003***	***0.133***	***0.049***	***0.168***	***0.008***	***0.016***	***0.084***	

971 Table A-5: Relative standard deviation (RSD) for trace element analysis in XRF determined on
972 BHVO-1, BIR-1, and BCR-1 basalts (Imai et al., 1995). Concentrations in weight percent.

	Ba	Ce	Co	Cr	Cu	Ga	La	Nb	Nd	Ni	Rb	Sc	Sr	V	Y	Zn	Zr
BHVO-1	***134.4***	***38.1***	***44.9***	***287.6***	***137.2***	***21.3***	***15.4***	***18.5***	***24.8***	***120.0***	***9.5***	***31.4***	***399.2***	***313.8***	***26.2***	***105.1***	***174.6***
Feb-19	133.7	37.0	45.9	284.0	162.5	21.7	13.4	19.5	23.0	125.9	10.1	29.1	396.1	307.3	27.3	123.5	181.0
Apr-19	141.0	37.1	45.0	282.9	158.9	21.7	14.1	19.6	24.2	126.9	10.3	29.6	396.6	309.9	26.9	121.8	180.7
Jun-19	137.2	37.8	43.7	285.7	160.3	21.4	12.2	19.5	23.5	126.3	10.2	30.2	397.0	310.2	27.2	121.9	181.3
Aug-19	145.3	42.4	46.2	282.5	157.8	22.5	17.3	19.6	25.3	127.4	10.6	30.6	395.9	308.4	26.9	124.1	179.1
Oct-19	132.8	41.6	44.2	285.3	158.1	22.3	15.4	19.4	24.7	126.8	10.4	30.9	396.8	310.1	27.2	122.3	179.4
Dec-19	142.2	36.9	45.5	284.8	155.4	21.3	14.9	19.4	24.5	127.6	10.5	30.6	395.6	308.7	27.1	123.2	179.4
Feb-20	141.5	40.0	46.1	283.6	157.4	22.2	13.9	19.6	22.8	124.1	10.7	28.8	397.1	310.9	28.2	122.7	179.7
Aug-20	139.9	37.4	45.5	281.6	167.0	20.0	12.8	19.6	23.0	127.5	10.2	29.5	397.2	310.0	27.7	123.7	181.6
RSD (%)	***3.1***	***5.7***	***2.0***	***0.5***	***2.3***	***3.7***	***11.3***	***0.4***	***3.9***	***0.9***	***2.1***	***2.6***	***0.2***	***0.4***	***1.6***	***0.7***	***0.5***
BIR-1	***6.8***	***1.9***	***52.2***	***392.9***	***120.7***	***15.5***	***0.6***	***0.6***	***2.4***	***168.9***	***0.2***	***43.2***	***108.6***	***320.6***	***15.6***	***70.4***	***14.8***
Feb-19	19.4	-0.5	50.1	382.9	129.2	16.0	2.2	2.9	1.3	171.2	2.7	39.8	108.6	321.9	16.7	69.9	15.8
Apr-19	20.2	-0.5	50.8	383.9	128.7	15.9	2.4	2.5	1.0	172.8	2.8	39.0	109.2	316.8	16.9	70.2	15.5
Jun-19	16.8	3.6	54.5	381.6	128.1	17.1	-0.7	2.4	3.7	171.1	2.4	40.5	109.5	320.4	17.2	68.8	15.6
Aug-19	19.5	-0.4	51.0	381.5	124.0	15.2	-1.5	2.6	2.5	174.4	2.5	38.3	109.4	319.1	16.6	68.2	14.5
Oct-19	17.1	-1.3	51.6	382.8	124.2	15.9	-2.1	2.9	1.3	173.7	2.6	40.4	109.6	320.3	16.9	69.7	14.5
Dec-19	17.2	5.8	53.0	385.6	124.2	15.5	-0.1	2.5	3.8	171.9	2.8	38.9	109.0	318.5	16.9	68.8	14.8
Feb-20	16.9	4.3	53.0	381.5	124.9	15.6	-1.1	2.4	1.8	171.7	2.9	39.6	109.0	318.7	17.5	69.5	14.4
Aug-20	19.5	1.5	50.4	386.1	133.2	16.0	-2.9	2.3	2.5	173.6	3.1	39.3	109.6	318.5	17.8	68.9	13.5
RSD (%)	***7.9***	***173.0***	***3.0***	***0.5***	***2.6***	***3.6***	***-416.0***	***8.3***	***48.2***	***0.7***	***8.4***	***1.9***	***0.3***	***0.5***	***2.5***	***1.0***	***5.2***
BCR-1	***683.3***	***53.9***	***37.6***	***13.5***	***19.6***	***22.2***	***25.5***	***12.7***	***28.7***	***11.7***	***46.6***	***32.4***	***334.9***	***404.4***	***36.9***	***128.5***	***190.3***
Feb-19	728.3	57.1	39.2	36.8	42.3	22.8	28.3	13.6	29.0	12.0	49.1	30.2	334.1	399.0	37.6	123.1	198.5
Apr-19	720.0	60.3	40.2	37.0	42.1	22.7	24.5	13.6	29.0	11.6	49.0	29.8	333.7	400.0	37.7	123.6	198.5
Jun-19	723.4	56.3	40.0	35.3	43.1	22.4	27.3	14.0	28.3	10.6	49.0	30.5	333.7	396.3	37.4	125.4	199.0
Aug-19	731.5	58.4	39.0	35.7	41.0	22.6	24.2	13.6	28.1	11.3	48.7	29.3	333.7	399.6	37.9	126.7	197.5
Oct-19	715.1	57.6	39.0	32.3	40.2	22.4	25.0	13.8	27.0	11.6	49.1	28.6	333.7	397.3	37.6	125.6	197.4
Dec-19	723.4	56.1	37.6	34.0	40.0	23.9	22.9	13.6	29.0	11.1	48.8	28.4	335.0	398.4	37.9	125.5	198.2
Feb-20	717.7	59.7	36.5	36.3	41.3	23.1	25.2	13.4	27.3	12.3	48.6	30.0	334.0	398.4	38.3	125.5	197.0
Aug-20	708.8	55.7	35.7	34.5	43.8	23.4	25.9	13.6	28.3	12.1	48.7	30.0	335.0	397.4	38.8	124.3	198.4
RSD (%)	***1.0***	***3.0***	***4.3***	***4.5***	***3.2***	***2.3***	***6.8***	***1.4***	***2.8***	***4.6***	***0.4***	***2.5***	***0.2***	***0.3***	***1.2***	***1.0***	***0.3***

973

974 Isocon Diagrams

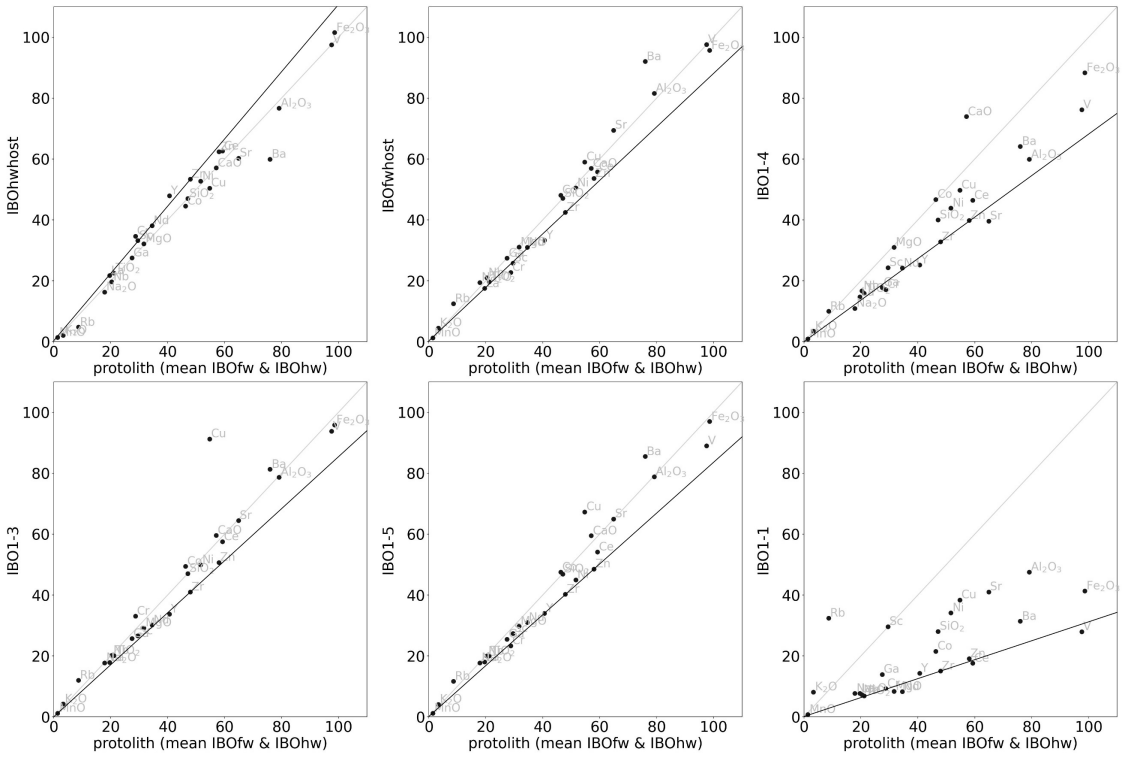

975

976 Figure A-1: Isocon diagrams for Í Botni fault rocks. IBOhwhost & IBOfwhost – hanging wall
977 and footwall host rock, IBO1-4 – breccia, IBO1-3 – protocataclasite, IBO1-5 – gouge, IBO1-1 –
978 calcite-cemented fault vein.
979

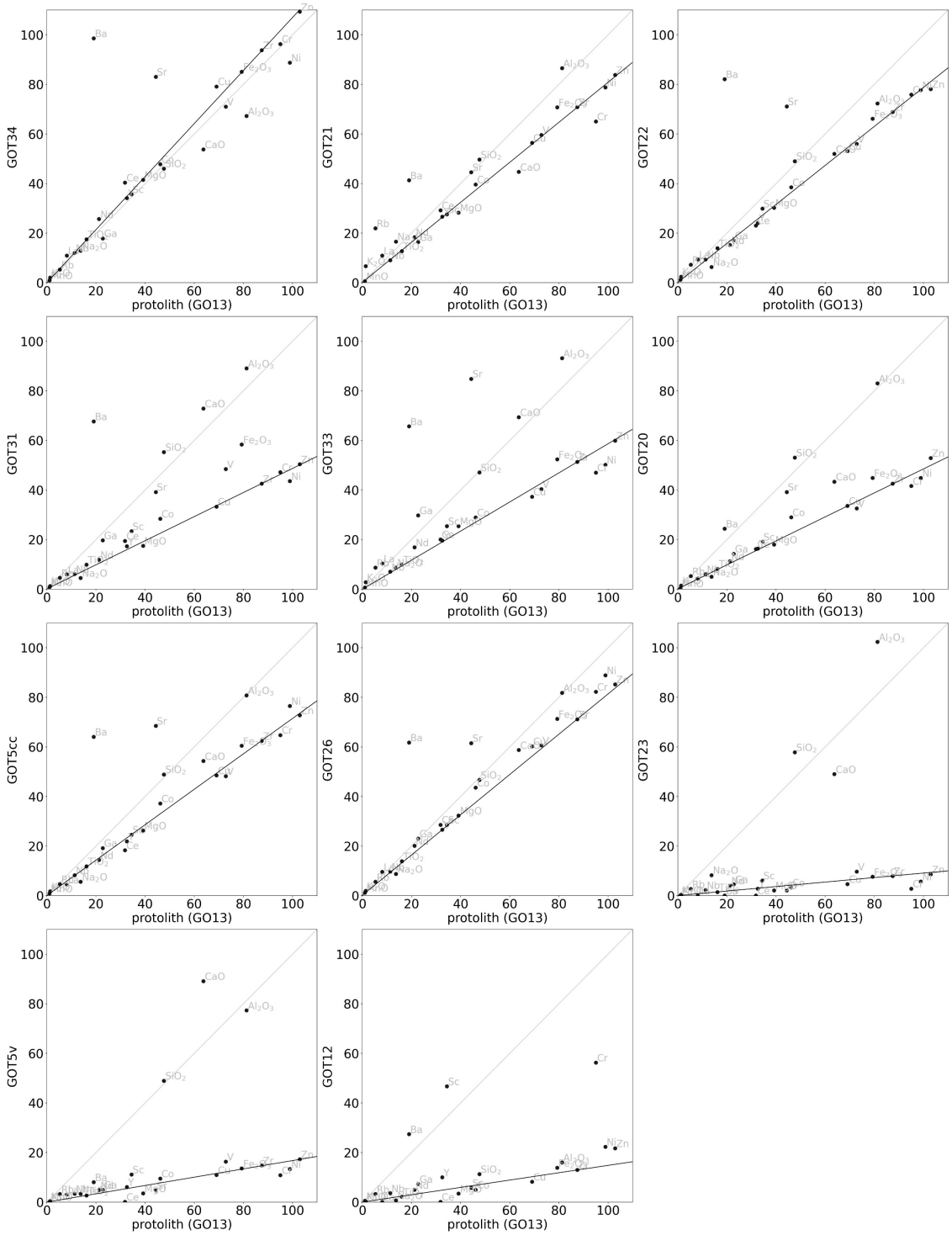

Figure A-2: Isocon diagrams for the Gøtugjógv fault rocks. GOT34 – far damage zone, GOT21 – near damage zone, GOT22 – breccia, GOT31 – protocataclasite, GOT33 – cataclasite, GOT20 – cataclasite, GOT5cc – ultracataclasite, GOT26 – ultracataclasite, GOT23 – zeolite vein, GOT12 – calcite fault vein.

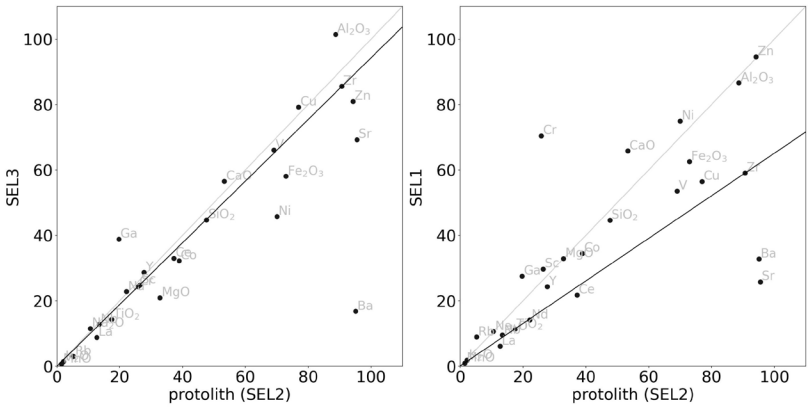

Figure A-3: Isocon diagrams for the Selatrað fault rocks. SEL3 – breccia/cataclasite, SEL1 – ultracataclasite.

Mass Balance Estimation

Table A-6: Mass balance calculation for the Gøtugjógv fault zone, estimating thickness of leached zone (in red, far ± near damage zone) required to provide amount of CaO, Al_2O_3, and SiO_2 gained by the fault core and the near damage zone, using Equation 3.3.

structure	sample	width	T_m			mass			
		meters	CaO	Al_2O_3	SiO_2	CaO	Al_2O_3	SiO_2	
far DZ	GO34		-0.212	-0.228	-0.098			leached	
near DZ	GO21	0.3	-0.132	0.315	0.288		0.09	0.09	
breccia	GO22	1.5	0.036	0.130	0.308	0.05	0.19	0.46	
proto-cc	GO31	0.1	0.399	1.098	1.288	0.04	0.11	0.13	
cataclasite	GO33	0.05	1.354	1.254	1.386	0.07	0.06	0.07	
cataclasite	GO5cc	0.3	0.194	0.393	0.439	0.06	0.12	0.13	
Ultra-cc	GO26	0.05	0.134	0.238	0.206	0.01	0.01	0.01	
zeolite vein	GO5v	0.05	7.276	4.625	5.080	0.36	0.23	0.25	
calcite vein	GO12	0.05	28.015	0.321	0.589	1.40	0.02	0.03	
						1.99	**0.84**	**1.17**	**added to core**
						-10.75 =mass/ (farDZ+0.5* nearDZ)/1.5	**-3.68** =mass/farDZ	**-11.97** =mass/farDZ	**m DZ leached**

References

Aggarwal, J., Palmer, M., Bullen, T., Arnórsson, S., and Ragnarsdóttir, K., 2000, The boron isotope systematics of Icelandic geothermal waters: 1. Meteoric water charged systems: Geochimica et Cosmochimica Acta, v. 64, no. 4, p. 579-585, https://doi.org/10.1016/S0016-7037(99)00300-2.

Ague, J. J., 1991, Evidence for major mass transfer and volume strain during regional metamorphism of pelites: Geology, v. 19, no. 8, p. 855-858, https://doi.org/10.1130/0091-7613(1991)019%3C0855:EFMMTA%3E2.3.CO;2.

Alt, J. C., and Honnorez, J., 1984, Alteration of the upper oceanic crust, DSDP site 417: mineralogy and chemistry: Contributions to Mineralogy and petrology, v. 87, no. 2, p. 149-169, https://doi.org/10.1007/BF00376221.

Arnórsson, S., 1995a, Geothermal systems in Iceland: Structure and conceptual models—I. High-temperature areas: Geothermics, v. 24, no. 5, p. 561-602, https://doi.org/10.1016/0375-6505(95)00025-9.

-, 1995b, Geothermal systems in Iceland: Structure and conceptual models—II. Low-temperature areas: Geothermics, v. 24, no. 5, p. 603-629, https://doi.org/10.1016/0375-6505(95)00026-7.

Arnórsson, S., and Barnes, I., 1983, The nature of carbon dioxide waters in Snaefellsnes, western Iceland: Geothermics, v. 12, no. 2-3, p. 171-176, https://doi.org/10.1016/0375-6505(83)90027-5.

Bamberg, B., 2023, Basaltic Fault Rock Petrology: Open Science Framework, https://osf.io/r3skf.

Bamberg, B., Walker, R., Reichow, M., and Ougier-Simonin, A., 2022, Fluid-driven cyclic reorganization in shallow basaltic fault zones: Geosphere, https://doi.org/10.1130/ges02488.1.

Bindeman, I. N., and Davis, A. M., 2000, Trace element partitioning between plagioclase and melt: investigation of dopant influence on partition behavior: Geochimica et Cosmochimica Acta, v. 64, no. 16, p. 2863-2878, https://doi.org/10.1016/S0016-7037(00)00389-6.

Boulton, C., Moore, D. E., Lockner, D. A., Toy, V. G., Townend, J., and Sutherland, R., 2014, Frictional properties of exhumed fault gouges in DFDP-1 cores, Alpine Fault, New Zealand: Geophysical Research Letters, v. 41, no. 2, p. 356-362, https://doi.org/10.1002/2013GL058236.

Carpenter, B. M., Ikari, M. J., and Marone, C., 2016, Laboratory observations of time-dependent frictional strengthening and stress relaxation in natural and synthetic fault gouges: Journal of Geophysical Research: Solid Earth, v. 121, no. 2, p. 1183-1201, https://doi.org/10.1002/2015JB012136.

Chalmers, J. A., and Waagstein, R., 2006, Scientific results from the deepened Lopra-1 borehole, Faroe Islands, Geological Survey of Denmark and Greenland, Danish Ministry of the Environment.

D'Antonio, M., and Kristensen, M., 2005, Hydrothermal alteration of oceanic crust in the West Philippine Sea Basin (Ocean Drilling Program Leg 195, Site 1201): inferences from a mineral chemistry investigation: Mineralogy and Petrology, v. 83, no. 1, p. 87-112, https://doi.org/10.1007/s00710-004-0060-6.

Das, A., and Krishnaswami, S., 2006, Barium in Deccan Basalt Rivers: its abundance, relative mobility and flux: Aquatic Geochemistry, v. 12, no. 3, p. 221-238, https://doi.org/10.1007/s10498-005-5856-4.

Deer, W. A., FRS, Howie, R. A., and Zussman, J., 2013, An Introduction to the Rock-Forming Minerals, Mineralogical Society of Great Britain and Ireland.

Eidesgaard, Ó. R., Schovsbo, N. H., Boldreel, L. O., and Ólavsdóttir, J., 2019, Shallow geothermal energy system in fractured basalt: A case study from Kollafjørður, Faroe Islands, NE-Atlantic Ocean: Geothermics, v. 82, p. 296-314, https://doi.org/10.1016/j.geothermics.2019.07.005.

Frolova, J., Ladygin, V., Rychagov, S., and Zukhubaya, D., 2014, Effects of hydrothermal alterations on physical and mechanical properties of rocks in the Kuril–Kamchatka island arc: Engineering Geology, v. 183, p. 80-95, https://doi.org/10.1016/j.enggeo.2014.10.011.

Gariépy, C., Ludden, J., and Brooks, C., 1983, Isotopic and trace element constraints on the genesis of the Faeroe lava pile: Earth and Planetary Science Letters, v. 63, no. 2, p. 257-272, https://doi.org/10.1016/0012-821X(83)90041-9.

Ghiara, M., Franco, E., Petti, C., Stanzione, D., and Valentino, G., 1993, Hydrothermal interaction between basaltic glass, deionized water and seawater: Chemical Geology, v. 104, no. 1-4, p. 125-138, https://doi.org/10.1016/0009-2541(93)90146-A.

Ghiara, M. R., Petti, C., Franco, E., Lonis, R., Luxoro, S., and Gnazzo, L., 1999, Occurrence of clinoptilolite and mordenite in Tertiary calc-alkaline pyroclastites from Sardinia (Italy): Clays and Clay Minerals, v. 47, no. 3, p. 319-328, https://doi.org/10.1346/CCMN.1999.0470308.

Gislason, S. R., and Eugster, H. P., 1987a, Meteoric water-basalt interactions. I: A laboratory study: Geochimica et Cosmochimica Acta, v. 51, no. 10, p. 2827-2840, https://doi.org/10.1016/0016-7037(87)90161-X.

-, 1987b, Meteoric water-basalt interactions. II: A field study in NE Iceland: Geochimica et Cosmochimica Acta, v. 51, no. 10, p. 2841-2855, https://doi.org/10.1016/0016-7037(87)90162-1.

Govindaraju, K., 1994, 1994 Compilation of working values and sample description for 383 geostandards: Geostandards Newsletter, v. 18, no. S1, p. 1-158, https://doi.org/10.1046/j.1365-2494.1998.53202081.x-i1.

Grant, J. A., 1986, The isocon diagram; a simple solution to Gresens' equation for metasomatic alteration: Economic Geology, v. 81, no. 8, p. 1976-1982, https://doi.org/10.2113/gsecongeo.81.8.1976.

Gratier, J. P., Renard, F., and Vial, B., 2014, Postseismic pressure solution creep: Evidence and time-dependent change from dynamic indenting experiments: Journal of Geophysical Research: Solid Earth, v. 119, no. 4, p. 2764-2779, https://doi.org/10.1002/2013JB010768.

Hadizadeh, J., 1994, Interaction of cataclasis and pressure solution in a low-temperature carbonate shear zone: Pure and Applied Geophysics, v. 143, no. 1, p. 255-280, https://doi.org/10.1007/BF00874331.

Haines, S. H., Kaproth, B., Marone, C., Saffer, D., and van der Pluijm, B., 2013, Shear zones in clay-rich fault gouge: A laboratory study of fabric development and evolution: Journal of Structural Geology, v. 51, p. 206-225, https://doi.org/10.1016/j.jsg.2013.01.002.

Hald, N., and Waagstein, R., 1991, The dykes and sills of the Early Tertiary Faeroe Island basalt plateau: Transactions of the Royal Society of Edinburgh: Earth Sciences, v. 82, no. 4, p. 373-388, https://doi.org/10.1017/S0263593300004211.

Hansen, H., Pedersen, A., Duncan, R., Bird, D., Brooks, C., Fawcett, J., Gittins, J., Gorton, M., and O'Day, P., 2002, Volcanic stratigraphy of the southern Prinsen af Wales Bjerge region, East Greenland: Geological Society, London, Special Publications, v. 197, no. 1, p. 183-218, https://doi.org/10.1144/GSL.SP.2002.197.01.08.

Hawkins, D. B., 1981, Kinetics of glass dissolution and zeolite formation under hydrothermal conditions: Clays and Clay Minerals, v. 29, no. 5, p. 331-340, https://doi.org/10.1346/CCMN.1981.0290503.

Hippertt, J., 1998, Breakdown of feldspar, volume gain and lateral mass transfer during mylonitization of granitoid in a low metamorphic grade shear zone: Journal of Structural Geology, v. 20, no. 2-3, p. 175-193, https://doi.org/10.1016/S0191-8141(97)00083-7.

Hjartarson, A., and Armannsson, H., Geothermal research in Greenland, *in* Proceedings World Geothermal Congress, Bali, Indonesia,°2010, p. 1-8.

Holm, P. M., Hald, N., and Waagstein, R., 2001, Geochemical and Pb–Sr–Nd isotopic evidence for separate hot depleted and Iceland plume mantle sources for the Paleogene basalts of the Faroe Islands: Chemical Geology, v. 178, no. 1-4, p. 95-125, https://doi.org/10.1016/S0009-2541(01)00260-1.

Hurwitz, S., Goff, F., Janik, C. J., Evans, W. C., Counce, D. A., Sorey, M. L., and Ingebritsen, S. E., 2003, Mixing of magmatic volatiles with groundwater and interaction with basalt on the summit of Kilauea Volcano, Hawaii: Journal of Geophysical Research: Solid Earth, v. 108, no. B1, https://doi.org/10.1029/2001JB001594.

Imai, N., Terashima, S., Itoh, S., and Ando, A., 1995, 1994 Compialtion of analytical data for minor and trace elements in seventeen GSJ geochemical reference samples, "Igneous Rock Series": Geostandards Newsletter, v. 19, no. 2, p. 135-213, https://doi.org/10.1111/j.1751-908X.1995.tb00158.x.

Jørgensen, O., 2006, The regional distribution of zeolites in the basalts of the Faroe Islands and the significance of zeolites as palaeotemperature indicators: Geological Survey of Denmark and Greenland Bulletin, v. 9, p. 123-156, https://doi.org/10.34194/geusb.v9.4865.

Kale, A., Bandela, N., Kulkarni, J., Sahoo, S. K., and Kumar, A., 2021, Hydrogeochemistry and multivariate statistical analysis of groundwater quality of hard rock aquifers from Deccan trap basalt in Western India: Environmental Earth Sciences, v. 80, no. 7, p. 1-24, https://doi.org/10.1007/s12665-021-09586-7.

Kristmannsdóttir, H., 1979, Alteration of Basaltic Rocks by Hydrothermal-Activity at 100-300 °C, Developments in Sedimentology, Volume 27, Elsevier, p. 359-367.

Kristmannsdóttir, H., and Tomasson, J., 1978, Zeolite Zones In Geothermal Areas in Iceland, *in* L.B. Sand, F. A. M., ed., Natural Zeolites: Occurrence, Properties, Use: Elmsford, New York, Pergamon Press, p. 277-284.

Lewis, A. L., Sarkar, B., Wade, P., Kemp, S. J., Hodson, M. E., Taylor, L. L., Yeong, K. L., Davies, K., Nelson, P. N., Bird, M. I., Kantola, I. B., Masters, M. D., DeLucia, E., Leake, J. R., Banwart, S. A., and Beerling, D. J., 2021, Effects of mineralogy, chemistry and physical properties of basalts on carbon capture potential and plant-nutrient element release via enhanced weathering: Applied Geochemistry, v. 132, p. 105023, https://doi.org/10.1016/j.apgeochem.2021.105023.

Marieni, C., Přikryl, J., Aradóttir, E. S., Gunnarsson, I., and Stefánsson, A., 2018, Towards 'green'geothermal energy: Co-mineralization of carbon and sulfur in geothermal reservoirs: International Journal of Greenhouse Gas Control, v. 77, p. 96-105, https://doi.org/10.1016/j.ijggc.2018.07.011.

Matter, J. M., Stute, M., Snæbjörnsdottir, S. Ó., Oelkers, E. H., Gislason, S. R., Aradottir, E. S., Sigfusson, B., Gunnarsson, I., Sigurdardottir, H., Gunnlaugsson, E., Axelsson, G., Alfredsson, H. A., Wolff-Boenisch, D., Mesfin, K., Taya, D. F. D. L. R., Hall, J., Dideriksen, K., and Broecker, W. S., 2016, Rapid carbon

mineralization for permanent disposal of anthropogenic carbon dioxide emissions: Science, v. 352, no. 6291, p. 1312-1314, http://doig.org/10.1126/science.aad8132.

Mattioli, M., Cenni, M., and Passaglia, E., 2016, Secondary mineral assemblages as indicators of multi stage alteration processes in basaltic lava flows: Evidence from the Lessini Mountains, Veneto Volcanic Province, Northern Italy: Periodico di Mineralogia, v. 85, p. 1-24, https://doi.org/10.2451/2015PM0375.

McInerney, F. A., and Wing, S. L., 2011, The Paleocene-Eocene Thermal Maximum: A perturbation of carbon cycle, climate, and biosphere with implications for the future: Annual Review of Earth and Planetary Sciences, v. 39, p. 489-516, https://doi.org/10.1146/annurev-earth-040610-133431.

Neuhoff, P. S., Fridriksson, T., and Bird, D. K. J. I. G. R., 2000, Zeolite parageneses in the north Atlantic igneous province: Implications for geotectonics and groundwater quality of basaltic crust, v. 42, no. 1, p. 15-44, https://doi.org/10.1080/00206810009465068.

Passey, S. R., and Bell, B. R., 2007, Morphologies and emplacement mechanisms of the lava flows of the Faroe Islands Basalt Group, Faroe Islands, NE Atlantic Ocean: Bulletin of Volcanology, v. 70, no. 2, p. 139-156, https://doi.org/10.1007/s00445-007-0125-6.

Passey, S. R., and Jolley, D. W., 2008, A revised lithostratigraphic nomenclature for the Palaeogene Faroe Islands Basalt group, NE Atlantic Ocean: Earth and Environmental Science Transactions of the Royal Society of Edinburgh, v. 99, no. 3-4, p. 127-158, https://doi.org/10.1017/S1755691009008044.

Philpotts, J. A., and Schnetzler, C. C., 1970, Phenocryst-matrix partition coefficients for K, Rb, Sr and Ba, with applications to anorthosite and basalt genesis: Geochimica et Cosmochimica Acta, v. 34, no. 3, p. 307-322, https://doi.org/10.1016/0016-7037(70)90108-0.

Proctor, B., Lockner, D., Kilgore, B., Mitchell, T., and Beeler, N., 2020, Direct evidence for fluid pressure, dilatancy, and compaction affecting slip in isolated faults: Geophysical Research Letters, v. 47, no. 16, p. e2019GL086767, https://doi.org/10.1029/2019GL086767.

Pytte, A., and Reynolds, R., 1989, The thermal transformation of smectite to illite, Thermal history of sedimentary basins, Springer, p. 133-140.

Rasmussen, J., and Noe-Nygaard, A., 1970, Geology of the Faeroe Islands: (Pre-Quaternary), Copenhagen, CA Reitzels.

Ritchie, J., and Hitchen, K., 1996, Early Paleogene offshore igneous activity to the northwest of the UK and its relationship to the North Atlantic Igneous Province: Geological Society, London, Special Publications, v. 101, no. 1, p. 63-78, https://doi.org/10.1144/GSL.SP.1996.101.01.04.

Schenato, F., Formoso, M., Dudoignon, P., Meunier, A., Proust, D., and Mas, A., 2003, Alteration processes of a thick basaltic lava flow of the Paraná Basin (Brazil): petrographic and mineralogical studies: Journal of South American Earth Sciences, v. 16, no. 5, p. 423-444, https://doi.org/10.1016/S0895-9811(03)00098-1.

Shimamoto, T., and Logan, J. M., 1981, Effects of simulated fault gouge on the sliding behavior of Tennessee sandstone: nonclay gouges: Journal of Geophysical Research: Solid Earth, v. 86, no. B4, p. 2902-2914, https://doi.org/10.1029/JB086iB04p02902.

Snæbjörnsdóttir, S. Ó., Sigfússon, B., Marieni, C., Goldberg, D., Gislason, S. R., and Oelkers, E. H., 2020, Carbon dioxide storage through mineral carbonation: Nature Reviews Earth & Environment, v. 1, no. 2, p. 90-102, https://doi.org/10.1038/s43017-019-0011-8.

Søager, N., and Holm, P. M., 2009, Extended correlation of the Paleogene Faroe Islands and East Greenland plateau basalts: Lithos, v. 107, no. 3-4, p. 205-215, https://doi.org/10.1016/j.lithos.2008.10.002.

-, 2011, Changing compositions in the Iceland plume; Isotopic and elemental constraints from the Paleogene Faroe flood basalts: Chemical Geology, v. 280, no. 3-4, p. 297-313, https://doi.org/10.1016/j.chemgeo.2010.11.017.

Stillings, M., Shipton, Z. K., and Lunn, R. J., 2023, Mechanochemical processing of silicate rocks to trap CO2: Nature Sustainability, 10.1038/s41893-023-01083-y.

Storey, M., Duncan, R. A., and Tegner, C., 2007, Timing and duration of volcanism in the North Atlantic Igneous Province: Implications for geodynamics and links to the Iceland hotspot: Chemical Geology, v. 241, no. 3, p. 264-281, https://doi.org/10.1016/j.chemgeo.2007.01.016.

Thomas, D., Paillet, F. L., and Conrad, M., 1996, Hydrogeology of the Hawaii Scientific Drilling Project borehole KP-1: 2. Groundwater geochemistry and regional flow patterns: Journal of Geophysical Research: Solid Earth, v. 101, no. B5, p. 11683-11694, https://doi.org/10.1029/95JB03845.

Tilling, R. I., and Jones, B. F., 1991, Composition of waters from the research drill hole at summit of Kilauea Volcano and of selected thermal and non-thermal groundwaters, Hawaii.

1166 Triana, R., Manuel, J., Herrera, R., Francisco, J., Ríos, R., Alberto, C., Castellanos, A., Mauricio, O., Henao, M., and
1167 Antonio, J., 2012, Natural zeolites filling amygdales and veins in basalts from the British Tertiary Igneous
1168 Province on the Isle of Skye, Scotland: Earth Sciences Research Journal, v. 16, no. 1, p. 41-53.
1169 Velde, B., and Vasseur, G., 1992, Estimation of the diagenetic smectite to illite transformation in time-temperature
1170 space: American Mineralogist, v. 77, no. 9-10, p. 967-976.
1171 Waagstein, R., Guise, P., and Rex, D. J. G. S., London, Special Publications, 2002, K/Ar and 39Ar/40Ar whole-rock
1172 dating of zeolite facies metamorphosed flood basalts: the upper Paleocene basalts of the Faroe Islands, NE
1173 Atlantic, v. 197, no. 1, p. 219-252, https://doi.org/10.1144/GSL.SP.2002.197.01.09.
1174 Waagstein, R., Hald, N., Jørgensen, O., Nielsen, P. H., Noe, A., Jørgensen, O., Noe-Nygaard, A., and Schonharting,
1175 G., 1984, Deep drilling on the Faeroe Islands: Bulletin of the Geological Society of Denmark, v. 32, p. 133-
1176 138.
1177 Walker, R. J., Holdsworth, R. E., Armitage, P. J., and Faulkner, D. R., 2013a, Fault zone permeability structure
1178 evolution in basalts: Geology, v. 41, no. 1, p. 59-62, https://doi.org/10.1130/G33508.1.
1179 Walker, R. J., Holdsworth, R. E., Imber, J., and Ellis, D., 2011, Onshore evidence for progressive changes in rifting
1180 directions during continental break-up in the NE Atlantic: Journal of the Geological Society, v. 168, no. 1, p.
1181 27-48, https://doi.org/10.1144/0016-76492010-021.
1182 Walker, R. J., Holdsworth, R. E., Imber, J., and Ellis, D., 2012, Fault-zone evolution in layered basalt sequences: A
1183 case study from the Faroe Islands, NE Atlantic margin: GSA Bulletin, v. 124, no. 7-8, p. 1382-1393,
1184 https://doi.org/10.1130/B30512.1.
1185 Walker, R. J., Holdsworth, R. E., Imber, J., Faulkner, D. R., and Armitage, P. J., 2013b, Fault zone architecture and
1186 fluid flow in interlayered basaltic volcaniclastic-crystalline sequences: Journal of Structural Geology, v. 51,
1187 p. 92-104, https://doi.org/10.1016/j.jsg.2013.03.004.
1188 Winter, J., 2001, An introduction to igneous and metamorphic petrology, Pearson, v. 552.1 W 784552.1 W 784552.1
1189 W 784552.1 W 784.
1190 Yukselen-Aksoy, Y., 2010, Characterization of two natural zeolites for geotechnical and geoenvironmental
1191 applications: Applied Clay Science, v. 50, no. 1, p. 130-136, https://doi.org/10.1016/j.clay.2010.07.015.
1192 Zen, E.-A., 1961, The zeolite facies; an interpretation: American Journal of Science, v. 259, no. 6, p. 401-409,
1193 https://doi.org/10.2475/ajs.259.6.401.
1194 Zviagina, B. B., Drits, V. A., and Dorzhieva, O. V., 2020, Distinguishing Features and Identification Criteria for K-
1195 Dioctahedral 1M Micas (Illite-Aluminoceladonite and Illite-Glauconite-Celadonite Series) from Middle-
1196 Infrared Spectroscopy Data: Minerals, v. 10, no. 2, p. 153.

1197